J. Fluid Mech. (2002), *vol.* 463, *pp.* 121–161.
DOI: 10.1017/S0022112002008674 Printed in the United Kingdom

Analysis of the radar reflectivity of aircraft vortex wakes

By KARIM SHARIFF AND ALAN WRAY
NASA Ames Research Center, Moffett Field, CA 94035, USA

(Received 5 July 2000 and in revised form 10 January 2002)

Radar has been proposed as a way of tracking wake vortices to reduce aircraft spacing and tests have revealed radar echoes from aircraft wakes in clear air. The mechanism causing refractive index gradients in these tests is thought to be the same as that for homogeneous and isotropic atmospheric turbulence in the Kolmogorov inertial range, for which there is a scattering analysis due to Tatarski. In reality, however, the structure of aircraft wakes has a significant coherent part superimposed with turbulence, about whose structure very little is known. This work adopts a picture of a coherent (in fact two-dimensional) wake to perform a scattering analysis and calculate the reflected power. In particular, two simple mechanisms causing refractive index gradients are considered: (A) radial pressure (and therefore density) gradient in a columnar vortex arising from the rotational flow; (B) adiabatic transport of atmospheric fluid within a descending oval surrounding a vortex pair. In the scattering analysis, Tatarski's weak scattering approximation is kept but the usual assumptions of a far field and a uniform incident wave are dropped. Neither assumption is generally valid for a wake that is coherent across the radar beam. For analytical insight, an approximate analysis that invokes, in addition to weak scattering, the far-field and wide cylindrical beam assumptions, is also developed and compared with the more general analysis. Reflectivities calculated for the oval (mechanism B) are within 2–13 dB m^2 of the measurements (≈ -70 dB m^2) of MIT Lincoln Laboratory at Kwajalein atoll. However, the present predictions have a cut-off away from normal incidence which is not present in the measurements. This implies that the two-dimensional picture is not entirely complete. Estimates suggest that the thin layer of vorticity which is baroclinically generated at the boundary of the oval is turbulent and this may account for reflectivity away from normal incidence. The reflectivity of a vortex (mechanism A) is comparable to that of the oval (mechanism B) but occurs at a frequency (about 50 MHz) that is lower than those considered in all the experiments to date. This result may be useful because: (i) existing atmospheric radars (known as ST radars) already operate at this frequency and so the present prediction could be verified; (ii) rain clutter is not a problem at this frequency; (iii) mechanism A is more robust because it is independent of atmospheric stratification.

1. Introduction

1.1. *Motivation*

The photographs of fluid motion in Van Dyke's (1982) album are all made possible by an optical effect in the visual range of the electromagnetic spectrum, for instance light scattering by smoke and the schlieren method. Fluid motions can also be 'visible' to radio waves: an article by Ottersten (1969) displays remarkable photographs of

atmospheric vortices imaged by radar in clear air. These include buoyant vortex rings, roll cells aligned with the wind in a stably stratified layer, and Kelvin–Helmholtz rollers in the tropopause. Perhaps one day we will also see radar photographs of aircraft wakes.

An important practical problem is that the vortex wakes of large aircraft pose a hazard to following aircraft and therefore, during instrument take-offs and landings, fixed distances are maintained between aircraft. These spacings are thought to be too conservative most of the time and to increase airport capacity NASA has set itself the goal of developing a system which dynamically sets the spacing (Perry, Hinton & Stuever 1997). Several elements comprise this system including computer simulation of wakes and vortex detection from the ground.

In the NASA effort, two methods of vortex detection are being concentrated upon: Doppler lidar at infrared frequencies and radar. Lidar is the more mature of the two and relies on scattering by aerosols. Field tests at airports using 10.6 μm lidar (Campbell *et al.* 1997; Köpp 1994) have detected vortices at ranges of up to 300 m; in clear weather this limit is set by the depth of focus of the optics. Hannon & Thomson (1994) report ranges of up to 4 km at 2.09 μm using high-energy pulsed lidar.

There are three motivations for considering radar. First is the concern that lidar cannot work in fog and rain due to absorption in the infrared range. Radar, on the other hand, is unaffected by rain and fog at sufficiently low frequencies. The second is that while lidar has adequate range to protect the modestly sized approach corridor currently set by the planners, radar has a potentially greater range. Third, optical systems tend to be more expensive to purchase and maintain than radar.

The present work focuses on *clear air* radar reflectivity of a vortex wake, that is, reflectivity in the absence of fog and rain droplets, both of which are strong scatterers.

1.2. *A thumbnail sketch of radar*

Radar transmits a radio signal and from the reflections received, rejects unwanted targets (clutter) by signal processing and determines the location of intended targets and their speed along the line of sight to the receiver. In the context of clear air detection of a wake, 'targets' are regions of the wake where there is a gradient of refractive index. The two candidate targets considered in this work are (A) the core of each vortex, which has a lower density and therefore lower index of refraction, and (B) the oval surrounding the vortex pair which transports atmospheric air from one altitude to another.

Each radar set usually operates at a single (carrier) frequency. The range to the target is determined from the time delay of the echo and the speed from its Doppler shift. This simple idea has reached a high level of maturity and some of its more interesting applications include Earth-based imaging of asteroids (e.g. Ostro *et al.* 2000) and Earth-based radar mapping of Mercury at a resolution of 15 km (Harmon *et al.* 1994).

The most common means of confining the transmission and reception to a narrow beam along a preferred direction is a reflecting dish with a small antenna at the focus. An array of antenna elements, arranged on the ground say, can also serve to form a beam. In this case, the beam can be pointed by varying the phase between individual elements. The larger the dish or array relative to the wavelength, the narrower the beam and the larger the power flux density (power per unit area) at the target. The power flux density (henceforth simply 'power density') at the target falls off as R_t^{-2}, where R_t is the range from the transmitter to the target.

There is a large catalogue of waveforms (amplitude and frequency modulations of

the carrier) which may be transmitted (Skolnik 1970, Chap. 3). The waveform can be a continuous wave (CW) or a pulse. The narrower the waveform in the time domain the better the range resolution but the speed resolution is worse, and conversely. If the range resolution is fine enough, individual regions of refractive index gradient within the wake may be discerned in the received signal. As reflections of a transmitted waveform are received, they are placed into range bins by sampling in time, and into Doppler bins by using a filter bank or a fast Fourier transform.

The receiver can either be co-located with the transmitter (the so-called monostatic case) or be separated (called bistatic).

The radar cross-section (RCS), the main quantity of interest in this work, is simply the power in the received signal, expressed so that it can be interpreted as the effective area that intercepts the incident flux and reflects it. It is thus a measure of the overall reflectivity of the target. We begin by defining it for the case of a time-harmonic wave. Suppose that the power density (per unit area) incident upon the target is uniformly $\bar{P}_{\mathrm{i,max}}$. Here $\bar{P}_{\mathrm{i,max}}$ is the time-averaged (spatial) maximum power density within the beam at the target. The radar cross-section, which has units of area, is defined such that:

$$\text{Time-averaged power scattered in the direction of the receiver} = \mathrm{RCS} \times \bar{P}_{\mathrm{i,max}}. \quad (1.1)$$

The time-averaged power density at the receiver will be $1/(4\pi R_{\mathrm{r}}^2)$ times the quantity on the left-hand side of (1.1) and so one has:

$$\mathrm{RCS} = 4\pi R_{\mathrm{r}}^2 \frac{\text{time-averaged power density at the receiver}}{\bar{P}_{\mathrm{i,max}}}. \quad (1.2)$$

Here R_{r} is the receiver to target distance. Once the RCS of a target is known, the transmitter power required to detect the target can be obtained (e.g. see § 7.1). Note that the RCS is the same whether the target is large and each part weakly reflective (like an aircraft wake) or small and each part highly reflective (like an insect).

1.3. *Previous theoretical work*

Currently, the means employed for calculating the clear-air reflectivity of aircraft wakes (Marshall & Myers 1996) and for interpreting the results of radar tests (Chadwick, Jordan & Detman 1984; Nespor *et al.* 1994) is the theory of Tatarski (1961) for scattering by refractive index fluctuations in atmospheric turbulence. The theory is based on the fact that in a turbulent velocity field the presence of mean vertical gradients of potential temperature and humidity lead to fluctuations in refractive index, $n(\boldsymbol{x})$. The velocity field is assumed to be statistically homogeneous and isotropic locally and to lie in the Kolmogorov inertial range. Refractive index gradients are therefore also homogeneous and isotropic. A basic result of Tatarski's scattering analysis (irrespective of the fluid mechanics) is that if the wavenumber of the incident radio wave is k, the only wavevector $\boldsymbol{k}_n$ of the refractive index capable of scattering to the observer is

$$\boldsymbol{k}_n = k(\hat{\boldsymbol{i}} - \hat{\boldsymbol{o}}), \quad (1.3)$$

where $\hat{\boldsymbol{i}}$ and $\hat{\boldsymbol{o}}$ are unit vectors in the directions respectively of the incident wave and the direction from the target to the observer. This is the so-called Bragg condition. In particular for backscattering ($\hat{\boldsymbol{o}} = -\hat{\boldsymbol{i}}$)

$$\boldsymbol{k}_n = 2k\hat{\boldsymbol{i}}. \quad (1.4)$$

Thus, the only flow wavevector which backscatters is aligned with the radar beam and has twice the radar wavenumber. Though derived using a Fourier integral, this result is understood intuitively by considering the requirement for constructive interference of two reflections of a single ray that are spaced $\lambda_n \equiv 2\pi/k_n$ apart: accounting for the round-trip, the second reflection lags the first by a distance $2\lambda_n$ and for constructive interference this must equal $m\lambda$, where m is an integer. For $m = 1$ the result is the same as (1.4). The requirement that the radar beam be aligned with the wavevector of refractive index comes about because if the wavefronts of $n(\boldsymbol{x})$ are tilted even slightly relative to the incident wave, then for every reflected ray there exists another ray that is phase shifted so as to exactly cancel it at the receiver.

After applying the scattering analysis to Kolmogorov turbulence, Tatarski's theory predicts that the radar cross-section per unit volume of isotropic turbulence in the inertial range is (e.g. see Ottersten 1969)

$$\eta = 0.38 C_n^2 \lambda^{-1/3}, \tag{1.5}$$

where λ is the radar wavelength and η has units of L^{-1}. The radar cross-section can thus be obtained if one knows C_n^2, the so-called second-order structure constant of refractive index fluctuations. Equation (1.5) has become incorporated into the aircraft vortex detection literature also, based on the belief that aircraft wake turbulence creates a turbulent energy cascade similar to atmospheric turbulence.

Marshall & Myers (1996) calculated C_n^2 as a function of position in a Reynolds-averaged calculation of a statistically two-dimensional vortex wake by using an algebraic closure relation for C_n^2 in the inertial range in terms of gradients of mean velocity and potential refractive index. This model is analogous to that given by Ottersten (1969, p. 1184) for atmospheric turbulence. No evaluation of radar cross-section was performed.

There are also classified reports cited by Gilson (1992) to which we were not privy.

1.4. *Present theoretical work*

The present work retains only Tatarski's weak scattering approximation but discards the rest of his development for the following reasons.

(i) The flow is not homogeneous isotropic turbulence. For instance, turbulence production is suppressed in the vortex cores (§ 6.1.2).

(ii) Tatarski's analysis assumes that a uniform plane wave is incident upon turbulence of infinite extent with the result that each unit volume produces a radar cross-section given by (1.5). To obtain the power scattered from a non-uniform beam, one would simply add the scattered powers from each part of the beam, assuming that the scattered fields of different parts are uncorrelated. This is the kind of assumption made in calculating the scattering due to a collection of rain drops. A vortex wake, on the other hand, always fills the incident beam in one direction and can have a coherence length that is comparable to the beam size. Thus one has to include variation of beam strength at the outset.

(iii) Tatarski's analysis also makes the assumption that the receiver is in the far field (Fraunhoffer zone) of the scattering region (or more precisely, in the far field of each region that may be considered uncorrelated with the rest). The condition that should be satisfied for this to hold is

$$\frac{\pi L_s^2}{\lambda R_r} \ll 1, \tag{1.6}$$

where L_s is the coherence length of the scattering region and λ is the wavelength. For homogeneous turbulence, L_s is about the size of an energy-containing eddy. However, for an index of refraction that is strongly correlated across the beam, $L_s \sim R_t\theta_b$ where θ_b is the e^{-1} half beamwidth. In particular, for co-located transmitter and receiver (1.6) becomes

$$\epsilon_{ff} = \frac{\pi R_r \theta_b^2}{\lambda} \ll 1. \tag{1.7}$$

Ironically therefore, the far-field condition becomes more difficult to satisfy the further one is from the target. Typical values of ϵ_{ff} in the experiments of Chadwick *et al.* (1984) and Gilson (1992) are $6 \leqslant \epsilon_{ff} \leqslant 15$; the far-field assumption is thus untenable if the wakes are coherent.

At any location downstream of the aircraft, the true state of the wake will lie somewhere between the fully coherent and fully turbulent extremes and in this paper we focus on the former extreme. To this end we assume that the wake is two-dimensional and drop the assumptions of a uniform incident beam and far field. One of the closing sections (§ 6) qualitatively discusses various three-dimensional phenomena and how they might affect the present predictions.

1.5. *Available experiments*

(i) Noonkester & Richter (1980) detected the wakes of departing aircraft using radar ($f = 3$ GHz, range $R = 100$–300 m). An interesting sinusoidal pattern was observed in the trace of target height (directly above the radar) versus time. They interpreted this to be hot engine exhaust spiralling around each vortex (and from the trace we were able to calculate the vortex circulation). Whether engine exhaust might be put to use for vortex detection during approach is briefly discussed in § 7.2.

(ii) Using a similar radar, Chadwick *et al.* (1984) detected the wakes of both departing and arriving aircraft but do not distinguish between the two in their results. The radar used was modest (200 W of power, 8 ft diameter dish) and the ranges were $R \leqslant 1$ km. The distribution functions of RCS in the atmosphere ahead of the plane and in the wake behind the plane overlapped a little and for positive identification of the wake, the authors suggested use of the spread in Doppler velocity. They suggested two mechanisms for scattering. First, they argued that aircraft vortices created a turbulent cascade similar to that assumed in the theory of atmospheric scattering (Tatarski 1961) but with a C_n^2 higher than that of the ambient atmosphere. The reflectivity lacked directional sensitivity which lent some credibility to the assumption of isotropy. Second, they suggested that heat and moisture from the engine further increase reflectivity.

(iii) Using a 1 MW pulse Doppler radar ($f = 5.6$ GHz, $R = 2.7$ km), Nespor *et al.* (1994) detected the vortices of a small fighter aircraft in approach configuration looking axially along the vortex.

(iv) So far, the best documented and controlled experiment and the one of direct relevance to this work was conducted by Lincoln Laboratory at Kwajalein atoll (Gilson 1992). The RCS of the wake of a C-5A was measured at a range of 15 km using powerful pulse Doppler radars having 2–7 MW of peak power. This experiment is remarkable in that simultaneous measurements were made at all six frequencies available in several radar sets installed at Kwajalein. Returns were detectable at five of these frequencies which ranged between 0.162 GHz and 5.7 GHz. There was no return at 35 GHz suggesting (from the Bragg condition (1.4)) that the smallest scale

responsible for scattering lies in the range $0.5 < \lambda_n < 2.6$ cm. From the observation that the radar cross-section was relatively flat as a function of frequency and dropped off somewhere above $f = 5.7$ GHz, Gilson concluded that particulates were not involved (they would give f^4 Rayleigh scattering). He noted that the frequency dependence was not the Kolmogorov $f^{1/3}$. The RCS decreased with altitude and vanished above the tropopause from which he concluded that the scattering mechanism was related to 'low altitude climate'. We will see later that that the relevant fact here is the decrease with altitude of the Brünt–Väisälä frequency, the measure of atmospheric density gradient relative to the adiabatic gradient. Gilson found that the RCS measured 1 km behind the plane was insensitive to engine thrust and the RCS measured at 10 000 ft altitude and 0.6 km behind the plane was insensitive to flap setting. He thus concluded that the main mechanism was 'turbulent mixing by the wake vortices of existing atmospheric index of refraction gradients'. There can pre-exist in the atmosphere both mean and turbulent gradients. This work attempts to predict the measured RCS by taking up the suggestion that atmospheric gradients play a role, assuming a calm atmosphere (and therefore only *mean* pre-existing gradients), and replacing 'turbulent mixing' with a simple picture of atmospheric air that is adiabatically compressed as it is transported downward within the oval surrounding the vortex pair.

(v) Finally, let us point out some interesting efforts aimed at detecting aircraft wakes using RASS (Radio Acoustic Sounding System), a technique that is now routinely used for profiling atmospheric winds. In RASS, radar is used to detect refractive index variations caused, remarkably, by sound waves launched into the wake as a tracer. The sound waves are scattered by the vortex flow and they in turn scatter an incident radio wave. The received radio signal is Doppler shifted about the sound speed. When the contribution of the speed of sound is subtracted out, the speed of the flow is revealed. There have been two studies. The first is reported in Iannuzzelli *et al.* (1998) and the second in Rubin (2000) and Rubin *et al.* (2000). The second seems promising. It uses a 915 MHz wind profiler. Rain and fog clutter is strong at this frequency; however, the vortex return is distinguishable from the clutter because it is Doppler shifted about the speed of sound. The sound frequency, chosen to satisfy the Bragg condition (1.3) is 2 KHz for the 915 MHz radar. At this frequency acoustic attenuation is about 16 dB km^{-1} which is rather strong.

1.6. *Outline of the paper*

Section 2 presents two laminar and two-dimensional mechanisms for producing refractive index variations and obtains the distributions of refractive index.

Given the index of refraction, in § 3 a scattering analysis using the Born weak scattering approximation is performed. We shall refer to this as the 'Born analysis'. This analysis has to be implemented numerically and so, for analytical insight, a simpler analysis (referred to as the 'approximate analysis') is presented in § 4. It introduces the simplifications of a far field and a cylindrical beam that is wider than the cross-sectional width of the target.

Section 5 presents numerical calculations for the radar cross-section, comparing the Born analysis, approximate analysis, and experiment. Section 6 presents a qualitative assessment of fluid dynamical effects not present in the two-dimensional picture and their implications for radar reflectivity. Section 7 presents some practical recommendations including sample characteristics for an ST (Stratospheric-Tropospheric) type radar that exploits mechanism A. Section 8 contains conclusions.

Aircraft	Weight W (lb)	Wingspan b (ft)	Vortex spacing b_0 (m)	Vortex circulation Γ ($m^2\,s^{-1}$)
Heavy commercial at approach	500 000	200	47.88	526
DC-8 (super 62,63) at approach	240 000	148.4	35.42	324.7
C-5A at 5000 ft	551 155	223	53.4	387.6

TABLE 1. Parameters of aircraft considered in this work.

2. Two mechanisms for refractive index variation

The refractive index n of humid air for frequencies below 20 GHz is given by Thayer (1974):

$$(n-1)\times 10^6 = 77.6\left(\frac{p_a}{T}\right) + 64.8\left(\frac{p_v}{T}\right) + 3.776\times 10^5\left(\frac{p_v}{T^2}\right). \tag{2.1}$$

Here p_a is the partial pressure (mb) of dry air, p_v is the partial pressure (mb) of water vapour and T is the temperature (K). The first two terms on the right-hand side of (2.1) are due to the induced polarization of air and water molecules, respectively. The third term is due to the permanent dipole moment of the water vapour molecule. The value of p_v can be obtained from the relative humidity, $\mathrm{RH} \equiv p_v/p_{\mathrm{sat}}$, where p_{sat} is the saturation pressure of water vapour and can be obtained as a function of temperature using the formula in Reid, Prausnitz & Poling (1987, p. 757). We will use rationalized MKS units (Jackson 1962, p. 611) throughout to write electrodynamic relationships. Then, for a non-magnetic material, $n = (\varepsilon/\varepsilon_0)^{1/2}$, where ε is the dielectric constant and the subscript '0' refers to vacuum.

Parameters of the three aircraft considered in this work are listed in table 1. The first is representative of a heavy commercial aircraft (Boeing 747-400 or Airbus 340) at sea level approach: the parameters were taken from Rennich (1997). Next is the smaller DC-8 also at sea level approach: the weight W is the design landing weight and the speed U is the full flaps speed at the given weight. Finally, there is the C-5A transport of the Lincoln Laboratory experiment at 5000 ft. The vortex separation, b_0, and vortex circulation, Γ, were obtained from the following standard relationships, both of which are derived using lifting line theory (Batchelor 1967, pp. 583–588) for an elliptically loaded wing:

$$b_0 = \frac{\pi b}{4}, \quad \Gamma = \frac{W}{\rho U b_0}. \tag{2.2}$$

The first relationship is deduced by equating the impulse of a point vortex pair to the lift (times speed) predicted by the theory, while the second is obtained by combining expressions for lift and circulation given by the theory.

2.1. *Mechanism A: radial density gradient in the vortex cores*

Mechanism A does not depend on atmospheric conditions. It arises simply from the fact that if the entropy is constant, the density in the core of a vortex is lower because the pressure is lower. Constancy of entropy is expected to hold due to lack of heating or cooling of the rolling-up boundary layer. The radial momentum equation (for laminar flow) together with the assumption of homentropic flow (p/ρ^γ = constant)

can be integrated to yield the radial density variation in each vortex:

$$\frac{\rho(r)}{\rho_\infty} = \left(1 - (\gamma - 1)\int_r^\infty \frac{1}{r}\frac{V_\theta^2}{c_\infty^2}\,\mathrm{d}r\right)^{1/(\gamma-1)}. \tag{2.3}$$

Here c_∞ and ρ_∞ are the ambient speed of sound and density, respectively. Equation (2.3) applies to both the density of water vapour and the density of air.

Two profiles of the circumferential velocity V_θ were considered. The first is the Spreiter–Sacks–Rankine (SSR) model where the velocity profile is that of the Rankine vortex,

$$V_\theta(r) = \frac{\Gamma}{2\pi r}\begin{cases} (r^2/r_0^2) & \text{for} \quad r < r_0, \\ 1 & \text{for} \quad r \geqslant r_0, \end{cases} \tag{2.4}$$

with core radius r_0 taking the Spreiter–Sacks (see Crow 1970) value of $r_0 = 0.0985 b_0$ which they obtained by equating the energy of a lifting line to that of a pair of Rankine vortices. The SSR model is known to overestimate the core size and to under-predict the maximum circumferential velocities when compared to flight measurements (see figure 1 in Widnall 1975). The second profile of circumferential velocity,

$$V_\theta = \frac{\Gamma}{2\pi\eta b_0}\begin{cases} 1189\eta^2 & \text{for } \eta < 0.0103, \\ [(1.27 + \log(\eta)/4)^{-14} + 1]^{-1/14} & \text{otherwise}, \end{cases} \tag{2.5}$$

was provided to us by Dr P. Spalart of Boeing; it represents his fit to flight observations and, when included in a vortex pair model, gives a close match to the energy of an elliptically loaded lifting line. Here

$$\eta \equiv \frac{r}{b_0}. \tag{2.6}$$

To compute the index of refraction, $n(r)$, within the vortex using (2.1) requires the temperature, $T(r)$, and partial pressures $p_a(r)$ and $p_v(r)$. Begin by obtaining ambient conditions: take $T_\infty = 288\,\mathrm{K}$ (for which $c_\infty = 341\,\mathrm{m\,s^{-1}}$) and from it obtain the saturation pressure in the ambient ($p_{\mathrm{sat},\infty}$) using the formula in Reid *et al.* (1987, p. 757). Multiplying $p_{\mathrm{sat},\infty}$ by the ambient relative humidity $(\mathrm{RH})_\infty$ (an input parameter) gives the vapour pressure in the ambient ($p_{v,\infty}$). Subtracting this from the total ambient pressure (which we took to be 1013.25 mb) gives the partial pressure of dry air in the ambient ($p_{a,\infty}$).

To obtain the partial pressures and temperature in the interior of the vortex, insert a velocity profile into (2.3), integrate numerically to obtain $\rho(r)/\rho_\infty$ and then compute the ratio $p(r)/p_\infty = (\rho(r)/\rho_\infty)^\gamma$. This ratio is the same for both vapour and dry air and when multiplied by the appropriate ambient values gives partial pressures, $p_a(r)$ and $p_v(r)$, in the vortex. Finally, to obtain the temperature use the ideal gas law: $T(r)/T_\infty = (P(r)/P_\infty)/(\rho(r)/\rho_\infty)$.

Figure 1 plots the relative change

$$\Delta\varepsilon_\mathrm{r} \equiv \frac{\varepsilon}{\varepsilon_\infty} - 1 = \frac{n^2}{n_\infty^2} - 1 \approx 2(n - n_\infty), \tag{2.7}$$

in dielectric constant from its ambient value (ε_∞). The approximation in (2.7) is based on the fact that $n = 1 + O(10^{-6})$. One observes that humidity has a weak influence (compare curves of the same line type with and without symbols). The solid and dotted curves compare $\Delta\varepsilon_\mathrm{r}$ for the SSR and Spalart profiles, respectively, for a heavy commercial airplane. The SSR profile results in a much less pronounced dip because of its underestimation of velocities in the core. For the DC-8, only the results (dashed

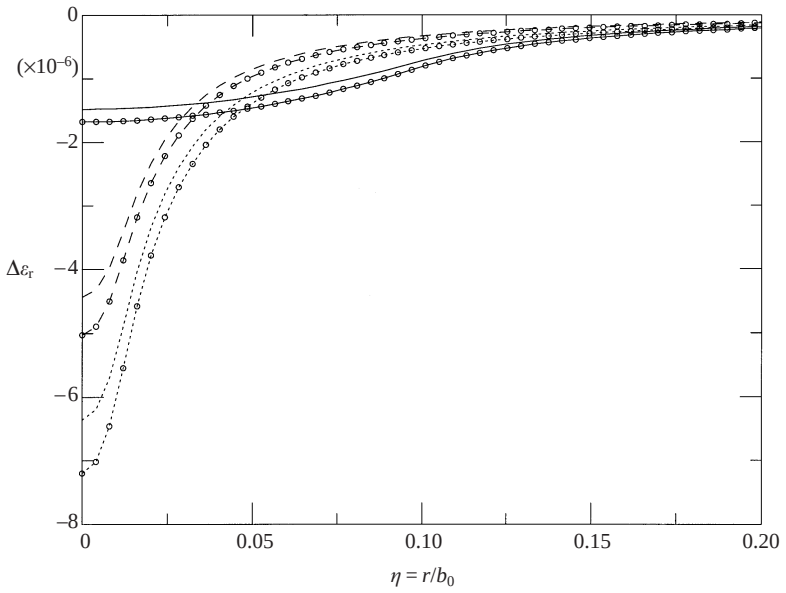

FIGURE 1. Distribution of $\Delta\varepsilon_r$ inside a vortex. Curves without symbols: dry air; curves with symbols: relative humidity, $(RH)_\infty = 80\%$; ——, SSR profile for the heavy aircraft; · · · · · ·, Spalart profile (2.5) for the heavy aircraft; – – – –, Spalart profile for the DC-8.

curves) for Spalart's profile are shown and we observe that the peak strength of $\Delta\varepsilon_r$ is diminished by about 30% compared to the heavy aircraft.

2.2. *Mechanism B: Transport of atmospheric fluid in the oval surrounding the vortices*

In § 2.2.1 the index of refraction inside a descending oval carrying atmospheric fluid is obtained and in § 2.2.2 its value for the Kwajalein experiment for later use in computing the RCS. This is followed in § 2.2.3 by a discussion of the qualitative experimental evidence that supports a role for a descending oval in radar scattering. A quantitative comparison with experiment will be presented later in the paper.

2.2.1. *A two-dimensional steady-flow picture*

Suppose that the vortex pair descends through a distance $\Delta z = z_f - z$ from its altitude of formation, z_f. As it descends, it carries around it an oval of ambient atmospheric fluid from z_f. The oval has semi-axes $1.045b_0$ and $0.865b_0$ (Milne-Thomson 1968, p. 360). In the scattering analysis we shall approximate the oval by a cylinder of circular cross-section of radius $a = 0.95b_0$ having a constant index of refraction inside.

Let tildes denote fluid properties within the oval and let overbars denote properties in the ambient atmosphere. Then introducing the total pressure, $p = p_a + p_v$, into (2.1), converting to SI units, and eliminating pressure in favour of density using the ideal gas law leads to the following equation for the difference in index of refraction between the oval and the surrounding atmosphere:

$$[\tilde{n}(z) - \bar{n}(z)] \times 10^6 = 223[\tilde{\rho}(z) - \bar{\rho}(z)] - 36.7[\tilde{\rho}_v(z) - \bar{\rho}_v(z)] + 1.08 \times 10^6 \left[\frac{\tilde{\rho}_v(z)}{\tilde{T}(z)} - \frac{\bar{\rho}_v(z)}{\bar{T}(z)}\right]. \tag{2.8}$$

Next we express (2.8) in terms of properties of the ambient atmosphere at level z.

As it descends, the fluid in the oval compresses adiabatically in response to increasing ambient pressure. A density difference, $\tilde{\rho}(z)-\bar{\rho}(z)$, from the ambient value will remain only if the ambient atmospheric density gradient is different from the adiabatic one. This difference is usually expressed in terms of the Brünt–Väisälä frequency N defined so that for small Δz (Pedlosky 1979)

$$\tilde{\rho}(z)-\bar{\rho}(z)=-\frac{\bar{\rho}(z)N^2}{g}\Delta z. \tag{2.9}$$

The first term in (2.8), which represents the dry air contribution is thus determined. For the second term write

$$\tilde{\rho}_v(z)-\bar{\rho}_v(z)=\bar{\rho}_v(z)\left(\frac{\tilde{\rho}_v(z)}{\bar{\rho}_v(z)}-1\right) \tag{2.10}$$

$$=\bar{\rho}_v(z)\left(\frac{\tilde{\rho}(z)}{\bar{\rho}(z)}-1\right) \tag{2.11}$$

$$=\frac{\bar{p}_v(z)\bar{\rho}(z)}{\bar{p}(z)}\left(\frac{\tilde{\rho}(z)}{\bar{\rho}(z)}-1\right) \tag{2.12}$$

$$=-\frac{\overline{RH}(z)p_{\mathrm{sat}}(\bar{T}_z)}{\bar{p}(z)}\frac{\bar{\rho}(z)N^2}{g}\Delta z. \tag{2.13}$$

Equation (2.11) is a consequence of combining the two expressions

$$\frac{\tilde{\rho}_v(z)}{\bar{\rho}_v(z_f)}=\frac{\tilde{\rho}(z)}{\bar{\rho}(z_f)},\quad \frac{\bar{\rho}_v(z)}{\bar{\rho}_v(z_f)}=\frac{\bar{\rho}(z)}{\bar{\rho}(z_f)}, \tag{2.14}$$

which express the fact that all constituents of the air compress by the same factor. The replacement of $\bar{\rho}_v(z)$ in (2.11) to obtain (2.12) is a consequence of the fact that all constituents of the ambient air are at the same temperature.

For the third term in (2.8) we use the fact that the oval and ambient pressures are equalized ($\tilde{\rho}\tilde{T}=\bar{\rho}\bar{T}$) so that (2.9) gives

$$\tilde{T}(z)=\bar{T}\left(1+\frac{N^2}{g}\Delta z\right), \tag{2.15}$$

to linear order in Δz. We may then write

$$\frac{\tilde{\rho}_v(z)}{\tilde{T}(z)}-\frac{\bar{\rho}_v(z)}{\bar{T}(z)}=-\frac{2\bar{\rho}_v(z)}{\bar{T}(z)}\frac{N^2}{g}\Delta z \tag{2.16}$$

$$=-\frac{2\overline{RH}(z)p_{\mathrm{sat}}(\bar{T}_z)}{\bar{p}(z)\bar{T}(z)}\frac{\bar{\rho}(z)N^2}{g}\Delta z. \tag{2.17}$$

The first equality uses (2.15) and (2.9), and the replacement of $\bar{\rho}_v(z)$ to obtain (2.17) is the same as in (2.12) and (2.13).

Putting all three terms together gives (in SI units)

$$[\tilde{n}(z)-\bar{n}(z)]\times 10^6=\frac{\bar{\rho}(z)N^2}{g}\Delta z\left[-223+\frac{\overline{RH}(z)}{\bar{p}(z)}(36.7-2.16\times 10^6/\bar{T}(z))\right]. \tag{2.18}$$

Note that the index of refraction jump across the oval is proportional to the stratification parameter N^2 and descent altitude Δz. The value of N near sea level varies from average summer levels of $0.014\,\mathrm{s}^{-1}$ through mild winter values of $0.02\,\mathrm{s}^{-1}$ to a value of $0.03\,\mathrm{s}^{-1}$ for a Fairbanks winter (W. D. Kriese, Boeing Aircraft, private

communication; Pedlosky 1979, p. 331). Since the index of refraction change across the oval diminishes with Δz, the wake will be undetectable by this mechanism for a sufficiently small wake descent. For the wake hazard problem what specification should one impose on the minimum Δz at which radar should be required to detect the oval? The lifetime of trailing vortices has been measured to range between 1.5 and 8 τ units (Spalart 1998, his figure 1) where one τ unit corresponds to the time taken for a vortex pair to descend one vortex separation distance. Hence the minimum separation in time between aircraft that could ever be contemplated (in the absence of techniques to destroy vortices) is 1.5 τ units. A vortex separation distance of $b_0 = 47.88$ m implies that the smallest descent for which the wake should be detectable is 72 m. This assumes that stratification neither impedes nor speeds the descent.

Using this value for Δz, we calculated $\Delta\varepsilon_r \approx 2\Delta n$ using $\bar{P}(z)$, $\bar{\rho}(z)$, and $\bar{T}(z)$ values for the Standard Atmosphere at sea level and $N = 0.017\,\mathrm{s}^{-1}$. For dry air we obtained $\Delta\varepsilon_r = -1.2 \times 10^{-6}$ while for 80% relative humidity, $\Delta\varepsilon_r = -1.7 \times 10^{-6}$, a small difference.

2.2.2. *Dielectric constant of the oval in the experiment* (*Gilson 1992*)

We chose the case (Gilson's run 15) having the lowest flight altitude (5000 ft). Note that Gilson (1992) presents results for this run in his figure 29 and figure 21 which is incorrectly labeled as run 16 (a similar error is present in table 6).

To secure a value for $\Delta\varepsilon_r$ we used the density and index of refraction vs. height sounding given in Gilson (1992). Since gradients relative to adiabatic are needed, one quantity had to be assumed to obtain them. This was the temperature at flight altitude which we took to be 295 K assuming a balmy sea level temperature of 85 °F and a lapse rate of $-0.005\,\mathrm{K\,m}^{-1}$. By comparing the measured index of refraction with the value for dry air at the local density we inferred that 7% relative humidity must have been present at flight altitude. The value of the Brünt–Väisälä frequency N was determined to be $0.017\,\mathrm{s}^{-1}$ by comparing the actual density gradient with the adiabatic one. We need the descent altitude of the oval 66 s after aircraft passage when all the radars show wake returns. For vortex pair descent unaffected by stratification, we find $\Delta z = 77$ m. The parameter determining the effect of stratification on vortex pair descent is $N_0^* = 2\pi N b_0^2/\Gamma$ (Spalart 1996). Its value is 0.79 and using Spalart's (1996) figures 4, 6 and 10(*a*), we concluded that stratification would shorten descent from 77 m to about 65 m. Thus we obtained $\Delta\varepsilon_r = -8.4 \times 10^{-7}$. As we will see, RCS $\propto \Delta\varepsilon_r^2$ so a factor of 2 error in this estimate would affect RCS by 6 dB.

2.2.3. *Experimental evidence*

Here we discuss facts immediately accessible from experiments that support the hypothesis that descending atmospheric fluid is responsible for radar scattering in those experiments. A more quantitative comparison will be presented later in the paper.

(i) Nespor *et al.* (1994, p. 658) noted that RCS tended to increase as the wake dropped into the lower beams. They interpreted this to mean growth of the turbulent region (so that a greater fraction of the radar pulse volume consisted of turbulence). However, the observations are more simply explained by the increasing refractive index contrast between the oval and the ambient as the oval descends.

(ii) Gilson notes that RCS decreases with altitude. This is consistent with the decrease in the Brünt–Väisälä frequency with altitude.

(iii) From the radar returns, Gilson (1992) was able to infer the length of the wake

along the radar beam (his figure 7 and data files he gave us). For run 15 the values generally lie in the range 80–120 m at 66 s (with one measurement of 150 m). These values are similar to the major axis of the oval (112 m).

(iv) At later times, however, the picture is not so simple. If the oval continued to descend at the same rate between 66 s and 235 s (Gilson's next measurement), we would expect RCS to increase by about 11 dB due to increasing density contrast between the oval and the surroundings. The measured raw RCS remains unchanged, however. This may be because stratification impedes descent of the oval. In particular, we have $N_0^* = 0.79$ for the experiment and figures 4, 6, 7 and 10 in Spalart (1996) show that between $N_0^* = 0.5$ and $N_0^* = 1$, there is a qualitative change in the descent of the vortices at 235 s (Spalart's $t = 5.08$). Whereas for the smaller value of N_0^*, the descent is only slightly impeded, for $N_0^* = 1$ the vortices bounce upward for a rectangular wing (Spalart's figure 4). For elliptical wing loading, the vortex pair separation decreases and it crashes through the oval leaving it considerably distorted near the altitude of formation. Such behaviour may account for the lack of increase in RCS. Furthermore, at about 235 s the wake lengths reported in the data file increase to 150–400 m. This may be due to turbulence in the boundary of the oval (§ 6.2.1).

In conclusion, it is clear that stratification is playing a role in the experiments and we believe that the simple picture of a descending oval provides a good model on which to base an initial quantitative study.

The next two sections present the scattering analysis. The physically motivated reader may safely skip to the results (§ 5).

3. Born scattering analysis

3.1. *General formulation*

Consider time-harmonic electric and magnetic fields

$$\bar{\boldsymbol{E}}(\boldsymbol{x}, t) = \mathrm{Re}[\boldsymbol{E}(\boldsymbol{x})\,\mathrm{e}^{-\mathrm{i}\omega t}], \quad \bar{\boldsymbol{H}}(\boldsymbol{x}, t) = \mathrm{Re}[\boldsymbol{H}(\boldsymbol{x})\,\mathrm{e}^{-\mathrm{i}\omega t}], \tag{3.1}$$

where $\boldsymbol{E}$ and $\boldsymbol{H}$ are complex. Later we will treat pulses by performing a Fourier synthesis of the results of the time-harmonic analysis.

The starting point to the solution of the scattering problem is the integral equation (Ishimaru 1978, vol. 1, p. 16):

$$\Pi_\mathrm{s}(\boldsymbol{x}) = \int_V \Delta\varepsilon_\mathrm{r}(\boldsymbol{x}')\boldsymbol{E}(\boldsymbol{x}')G(\boldsymbol{x}, \boldsymbol{x}')\,\mathrm{d}\boldsymbol{x}', \tag{3.2}$$

$$\Delta\varepsilon_\mathrm{r}(\boldsymbol{x}') \equiv \frac{\varepsilon(\boldsymbol{x}')}{\varepsilon_0} - 1. \tag{3.3}$$

Here

$$G(\boldsymbol{x}, \boldsymbol{x}') = \frac{\mathrm{e}^{\mathrm{i}k\Delta}}{4\pi\Delta}, \quad \Delta \equiv |\boldsymbol{x} - \boldsymbol{x}'|, \tag{3.4}$$

is the free-space Green's function and Π_s is the Hertz vector of the scattered field such that

$$\boldsymbol{E}_\mathrm{s} = \nabla \times \nabla \times \Pi_\mathrm{s}, \quad \boldsymbol{H}_\mathrm{s} = -\mathrm{i}\omega\varepsilon_0 \nabla \times \Pi_\mathrm{s}. \tag{3.5}$$

The integral in (3.2) has a simple interpretation: each point scatters a spherical wave (represented by G) whose Hertz vector has the same phase and direction as the local electric field but with amplitude diminished by $\Delta\varepsilon_\mathrm{r}$. The problem is an integral

equation because each scattered wave changes the electric field, is re-scattered and so on *ad infinitum*.

To calculate $\boldsymbol{E}_s$ and $\boldsymbol{H}_s$ from Π_s requires evaluating curls (with respect to $\boldsymbol{x}$) of the integrand in (3.2). We list them here for completeness. Defining $\boldsymbol{C} \equiv \Delta\varepsilon_r(\boldsymbol{x}')\boldsymbol{E}(\boldsymbol{x}')$, the vector in the integrand which is constant with respect to $\boldsymbol{x}$, we obtain

$$\nabla \times \boldsymbol{C}G = \nabla G \times \boldsymbol{C}, \tag{3.6}$$

$$\nabla \times \nabla \times \boldsymbol{C}G = \nabla \times (\nabla G \times \boldsymbol{C}) = (\boldsymbol{C} \cdot \nabla)\nabla G - \boldsymbol{C}\nabla^2 G. \tag{3.7}$$

Equations (3.6) and (3.7) involve first and second derivatives of G:

$$\frac{\partial G}{\partial x_i} = \frac{1}{4\pi}\frac{e^{ik\Delta}}{\Delta^2}x_i(ik - 1/\Delta), \tag{3.8}$$

$$\frac{\partial^2 G}{\partial x_i \partial x_j} = \frac{1}{4\pi}\frac{e^{ik\Delta}}{\Delta^4}[(\Delta^2\delta_{ij} + ikx_ix_j\Delta - 2x_ix_j)(ik - 1/\Delta) + x_ix_j/\Delta], \tag{3.9}$$

where δ_{ij} is the Kronecker delta.

3.2. *The Born approximation*

The integrand in (3.2) contains the total electric field (incident + scattered) which is in general unknown; however, since in the present case $\Delta\varepsilon_r = O(10^{-6})$ one can invoke the Born approximation that it can be set equal to the incident field. This corresponds to retaining only the first of multiple scatterings, or mathematically, to keeping only the first term in a Neumann series solution to the integral equation. The Born approximation is valid when the scattered electric field is much smaller than the incident field in the region of the target. Equations (3.2), (3.7) and (3.9) imply that the following three conditions have to be satisfied for this to be true:

$$\Delta\varepsilon_r\{1, kL_s, (kL_s)^2\} \ll 1. \tag{3.10}$$

It should be noted that Ishimaru (1978) gives only the second condition, perhaps because he was thinking of scattering by particles smaller than a wavelength. In that case $kL_s < 1$ and the second condition is the more stringent one.

3.3. *Calculation of the radar cross-section for the time-harmonic analysis*

The definition of radar cross-section given earlier (1.2) is

$$\mathrm{RCS} = 4\pi R_r^2 \frac{\text{time-averaged power density at the receiver}}{\bar{P}_{i,\max}}. \tag{3.11}$$

The time-averaged received power density vector is

$$\boldsymbol{S}_s(\boldsymbol{x}) = \tfrac{1}{2}\mathrm{Re}\{\boldsymbol{E}_s(\boldsymbol{x}) \times \boldsymbol{H}_s^*(\boldsymbol{x})\}, \tag{3.12}$$

where Re denotes the real part. The numerator in (3.11) was evaluated as $|\boldsymbol{S}_s(\boldsymbol{x})|$ and (as a check) $\boldsymbol{S}_s(\boldsymbol{x}) \cdot \hat{\boldsymbol{o}}$ where $\hat{\boldsymbol{o}}$ is a unit vector (defined in (3.21) below) from the target to the receiver. Differences between the two evaluations were very slight.

Appendix A, § A.1 shows that the denominator in (1.2) is simply $(1/2)c\varepsilon_0$.

3.4. *Coordinate systems*

We choose the coordinate system of $\boldsymbol{x}$ and $\boldsymbol{x}'$ in the integral (3.2) to be located on the axis of the target as shown in figure 2. In particular, the origin of the coordinate system is chosen so that the beam centreline intersects the (x, y)-plane at $(x = 0, y = y_0)$, y_0 being the beam pointing error.

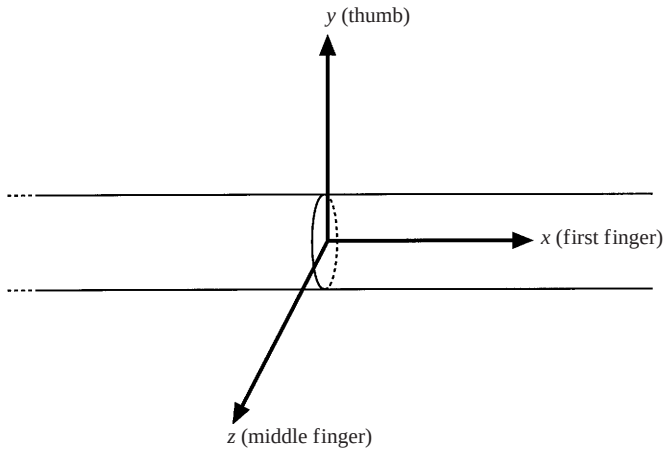

FIGURE 2. Wake coordinate system. Use the indicated fingers of the left hand to follow the transformations (3.13)–(3.15).

Appendix A gives the electric field in the incident beam using coordinates centred on the antenna aperture. Hence we need to transform target coordinates (x, y, z) to aperture coordinates (x^*, y^*, z^*).

Imagine that the transmitter is looking at the wake from the same side as the reader is looking at figure 2. This figure shows which fingers of the left hand the reader may employ to visualize the transformations. The reader's palm will eventually become the plane of the aperture, the middle finger being the direction of propagation, and the first finger the direction of polarization. The first transformation turns z (the middle finger) away from the reader so that it can eventually become the beam axis. The next transformation shifts the origin to $(x = 0, y = y_0)$ to ensure that the beam axis intersects the (x, y)-plane where we want it. The resulting coordinates are therefore

$$\begin{pmatrix} x^{(1)} \\ y^{(1)} \\ z^{(1)} \end{pmatrix} = \begin{pmatrix} -x \\ y - y_0 \\ -z \end{pmatrix}. \tag{3.13}$$

Next, rotate the coordinate system counter-clockwise by angle $\beta_t \in [0, 2\pi]$ around the $x^{(1)}$-axis (first finger). Thus β_t is an elevation angle to the target. Follow this by a counter-clockwise $\alpha_t \in [-\pi/2, \pi/2]$ rotation about the current y-axis (thumb). Next, translate the coordinate system in the negative z-direction by the range R_t from the transmitter to the point $\boldsymbol{x} = (0, y_0, 0)$ on the target. These three transformations give

$$\begin{pmatrix} x^{(2)} \\ y^{(2)} \\ z^{(2)} \end{pmatrix} = \begin{pmatrix} \cos\alpha_t & 0 & -\sin\alpha_t \\ 0 & 1 & 0 \\ \sin\alpha_t & 0 & \cos\alpha_t \end{pmatrix} \begin{pmatrix} 1 & 0 & 0 \\ 0 & \cos\beta_t & -\sin\beta_t \\ 0 & \sin\beta_t & \cos\beta_t \end{pmatrix} \begin{pmatrix} -x \\ y - y_0 \\ -z \end{pmatrix} + \begin{pmatrix} 0 \\ 0 \\ R_t \end{pmatrix}. \tag{3.14}$$

Finally, to orient the polarization vector along the x^*-axis (first finger), the coordinate system is rotated by angle γ about the $z^{(2)}$-axis (about the middle finger, counter-clockwise looking into the palm):

$$\begin{pmatrix} x^* \\ y^* \\ z^* \end{pmatrix} = \begin{pmatrix} \cos\gamma & \sin\gamma & 0 \\ -\sin\gamma & \cos\gamma & 0 \\ 0 & 0 & 1 \end{pmatrix} \begin{pmatrix} x^{(2)} \\ y^{(2)} \\ z^{(2)} \end{pmatrix}. \tag{3.15}$$

Putting all the transformations together gives

$$x^* = \cos\gamma\{-x\cos\alpha_t - \sin\alpha_t[(y-y_0)\sin\beta_t - z\cos\beta_t]\} + \sin\gamma\{(y-y_0)\cos\beta_t + z\sin\beta_t\}, \quad (3.16)$$

$$y^* = \cos\gamma\{(y-y_0)\cos\beta_t + z\sin\beta_t\} - \sin\gamma\{-x\cos\alpha_t - \sin\alpha_t[-z\cos\beta_t + (y-y_0)\sin\beta_t]\}, \quad (3.17)$$

$$z^* = R_t - x\sin\alpha_t + \cos\alpha_t[-z\cos\beta_t + (y-y_0)\sin\beta_t]. \quad (3.18)$$

The incident electric field is in the $\hat{\boldsymbol{x}}^*$-direction and to obtain its (x, y, z) components for use in the integral (3.2) we note that

$$\hat{\boldsymbol{x}}^* = -\cos\alpha_t\cos\gamma\hat{\boldsymbol{x}} + (\cos\beta_t\sin\gamma - \cos\gamma\sin\alpha_t\sin\beta_t)\hat{\boldsymbol{y}} + (\sin\beta_t\sin\gamma + \cos\gamma\sin\alpha_t\cos\beta_t)\hat{\boldsymbol{z}}, \quad (3.19)$$

from (3.16). Like the 'incident direction' $\hat{\boldsymbol{i}}$ from the transmitter to the point $(0, y_0, 0)$

$$\hat{\boldsymbol{i}} = \hat{\boldsymbol{z}}^* = -\sin\alpha_t\hat{\boldsymbol{x}} + \cos\alpha_t\sin\beta_t\hat{\boldsymbol{y}} - \cos\alpha_t\cos\beta_t\hat{\boldsymbol{z}}, \quad (3.20)$$

we define the 'observer direction' $\hat{\boldsymbol{o}}$ from the point $(0, y_0, 0)$ to the receiver in a similar way using angles α_r and β_r and reversing the sign of the vector:

$$\hat{\boldsymbol{o}} = \sin\alpha_r\hat{\boldsymbol{x}} - \cos\alpha_r\sin\beta_r\hat{\boldsymbol{y}} + \cos\alpha_r\cos\beta_r\hat{\boldsymbol{z}}. \quad (3.21)$$

The location of the receiver is then:

$$\boldsymbol{x}_r = y_0\hat{\boldsymbol{y}} + R_r\hat{\boldsymbol{o}}. \quad (3.22)$$

3.5. *Numerical integration procedure*

Two methods were used to evaluate the integral (3.2) which gives the scattered field.

Method A: This is the more general but less efficient of the two methods. It uses Simpson's rule in cylindrical coordinates (x, r, ϕ). The integral over the infinite direction x was truncated at $|x| = 3u_b$, where $u_b = R_t\sin\theta_b$ is the characteristic beam radius at the target. In the radial direction, the integrals were truncated at $r = 0.5b_0$ when the vortex was the target. When the oval is the target, the integrand is zero for $r > a$. The number of quadrature points in each direction was determined from the input parameter N_{ql}, which is the number of quadrature intervals desired per characteristic length l of fluctuations of the integrand. The characteristic length in each direction was chosen as

$$l_x = \min(\lambda, u_b), \quad l_\phi = \min(\lambda, u_b), \quad l_r = \min(\lambda, u_b, \delta_r), \quad (3.23)$$

where

$$\delta_r = \begin{cases} \delta_\varepsilon & \text{if the vortex is the target,} \\ \frac{1}{2}a & \text{if the oval is the target.} \end{cases} \quad (3.24)$$

Here δ_ε is the radius where $\Delta\varepsilon_r(r)$ reaches half its peak value. If the length of an integration is L then $N_l = \text{int}(L/l) + 1$ characteristic lengths cover the integration length and the number of quadrature intervals was determined as $N_q = N_{ql}\max(3, N_l)$, the purpose of the max being to ensure a minimum number of quadrature points. For each calculation of radar cross-section presented for this method we used $N_{ql} = 8$ and accepted the result if $N_{ql} = 16$ showed no perceptible change in radar cross-section. Computational cost prevented use of this method above $f \approx 0.16\,\text{GHz}$.

Method B: This method was developed to efficiently calculate the radar cross-section for the oval at the relatively high frequencies of the test at Kwajalein. The

implementation is currently specialized to backscattering at normal incidence for the oval.

Each of the six integrals needed to evaluate the scattered $\boldsymbol{E}$ and $\boldsymbol{H}$ fields is of the form

$$I = \int A(x, y, z)\, \mathrm{e}^{\mathrm{i}\phi(x,y,z)}\, \mathrm{d}x\, \mathrm{d}y\, \mathrm{d}z, \tag{3.25}$$

where z is the direction along the beam axis and the cross-beam coordinates are (x, y). The basic idea of the method is to divide the integration interval in a given direction (say ζ) into many sub-intervals and to approximate the amplitude and phase in each sub-interval as a linear function of ζ:

$$I = \int_{\zeta_1}^{\zeta_2} A(\zeta)\, \mathrm{e}^{\mathrm{i}\phi(\zeta)}\, \mathrm{d}\zeta \approx \Delta\zeta \int_0^1 (A(\zeta_1) + \xi \Delta A)\, \mathrm{e}^{\mathrm{i}(\phi(\zeta_1)+\xi\Delta\phi)}\, \mathrm{d}\xi, \tag{3.26}$$

where

$$\Delta A \equiv A(\zeta_2) - A(\zeta_1), \quad \Delta\phi \equiv \phi(\zeta_2) - \phi(\zeta_1). \tag{3.27}$$

The integral in each sub-interval can then be obtained analytically:

$$I \approx -\frac{\mathrm{i}}{\Delta\phi}\Delta\zeta \left\{ -\left[A(\zeta_1) + \frac{\mathrm{i}}{\Delta\phi}\Delta A\right] \mathrm{e}^{\mathrm{i}\phi(\zeta_1)} + \left[A(\zeta_2) + \frac{\mathrm{i}}{\Delta\phi}\Delta A\right] \mathrm{e}^{\mathrm{i}\phi(\zeta_2)} \right\}. \tag{3.28}$$

The integral along the beam (z-direction) was performed first and tests revealed that one sub-interval was sufficient to obtain an accurate integral. This is due to uniformity of the dielectric constant and slow variation of the strength of the incident beam. A model with a slice of entrained ambient fluid will also be treated (figure 6). For this case, one interval along the beam for each of the two regions was used. For each interval, the resulting integral has the form (3.28) with ζ replaced by z. Now the two terms in the result (3.28), when considered as functions of the remaining coordinates, are again in the basic form (3.25) with amplitudes and phases a function of x and y. Hence, the same method can be applied successively in these directions. In these directions, hundreds of sub-intervals were required for convergence.

4. Approximate scattering analysis

4.1. *General formulation*

To obtain analytical insight into the numerical results and as a check on the numerics, it is useful to have closed-form expressions which provide the radar cross-section in certain limits. Such expressions are developed in this section and, later in the paper, their predictions will be compared with the formulation of the previous section.

Four assumptions will be invoked. First is the far-field assumption which holds when (1.6) is satisfied. In this case

$$G = \frac{\mathrm{e}^{\mathrm{i}kR_\mathrm{r}}}{4\pi R_\mathrm{r}} \mathrm{e}^{-\mathrm{i}k\boldsymbol{x}'\cdot\hat{\boldsymbol{o}}}, \tag{4.1}$$

and the scattered electric field implied by (3.2) is given by (see Ishimaru 1978, vol. 1, p. 17)

$$\boldsymbol{E}_\mathrm{s}(\boldsymbol{x}) = \boldsymbol{f}(\hat{\boldsymbol{o}}, \hat{\boldsymbol{i}})\, \mathrm{e}^{\mathrm{i}kR_\mathrm{r}}/R_\mathrm{r}, \tag{4.2}$$

$$\boldsymbol{f}(\hat{\boldsymbol{o}}, \hat{\boldsymbol{i}}) \equiv \frac{k^2}{4\pi} \int_V \{-\hat{\boldsymbol{o}} \times [\hat{\boldsymbol{o}} \times \boldsymbol{E}(\boldsymbol{x}')]\} \Delta\varepsilon_\mathrm{r}(\boldsymbol{x}')\, \mathrm{e}^{-\mathrm{i}k\boldsymbol{x}'\cdot\hat{\boldsymbol{o}}}\, \mathrm{d}\boldsymbol{x}'. \tag{4.3}$$

The second assumption is the Born approximation of the previous section: $\boldsymbol{E}(\boldsymbol{x}') \longrightarrow \boldsymbol{E}_{\mathrm{i}}(\boldsymbol{x}')$ in the integrand.

The third approximation replaces the conical incident beam by a cylindrical beam in the vicinity of the target as explained in Appendix A, § A.2. The incident electric field then has the form

$$\boldsymbol{E}_{\mathrm{i}}(\boldsymbol{x}) = \hat{\boldsymbol{x}}^* F(u;\sigma)\, \mathrm{e}^{\mathrm{i}kz^*}, \tag{4.4}$$

where

$$u \equiv \left(x^{*2} + y^{*2}\right)^{1/2} \tag{4.5}$$

is the normal distance from the beam axis. Substituting for z^* from (3.18) and using (3.20), the incident electric field takes the form

$$\boldsymbol{E}_{\mathrm{i}}(\boldsymbol{x}) = \hat{\boldsymbol{x}}^* F(u;\sigma)\, \mathrm{e}^{\mathrm{i}k\boldsymbol{x}\cdot\hat{\boldsymbol{i}}}\, \mathrm{e}^{\mathrm{i}k\Phi}, \tag{4.6}$$

where

$$\Phi \equiv R_{\mathrm{t}} - y_0 \cos\alpha_{\mathrm{t}} \sin\beta_{\mathrm{t}}. \tag{4.7}$$

Substituting (4.6) into (4.3) gives

$$\boldsymbol{f}(\hat{\boldsymbol{o}}, \hat{\boldsymbol{i}}) = \frac{\boldsymbol{s}k^2 \mathrm{e}^{\mathrm{i}k\Phi}}{4\pi} \int_V \Delta\varepsilon_{\mathrm{r}}(\boldsymbol{x}') F(u;\sigma)\, \mathrm{e}^{\mathrm{i}k\boldsymbol{x}'\cdot(\hat{\boldsymbol{i}}-\hat{\boldsymbol{o}})}\, \mathrm{d}\boldsymbol{x}', \tag{4.8}$$

where

$$\boldsymbol{s} \equiv -\hat{\boldsymbol{o}} \times [\hat{\boldsymbol{o}} \times \hat{\boldsymbol{x}}^*]. \tag{4.9}$$

Let us keep ready at hand the following geometric quantity which appears in (4.8):

$$\boldsymbol{x}\cdot(\hat{\boldsymbol{i}} - \hat{\boldsymbol{o}}) = -Px - Qy - Sz, \tag{4.10}$$

where

$$P \equiv \sin\alpha_{\mathrm{t}} + \sin\alpha_{\mathrm{r}}, \tag{4.11}$$

$$Q \equiv -\cos\alpha_{\mathrm{t}} \sin\beta_{\mathrm{t}} - \cos\alpha_{\mathrm{r}} \sin\beta_{\mathrm{r}}, \tag{4.12}$$

$$S \equiv \cos\alpha_{\mathrm{t}} \cos\beta_{\mathrm{t}} + \cos\alpha_{\mathrm{r}} \cos\beta_{\mathrm{r}}. \tag{4.13}$$

Two types of cylindrical beams, justified in Appendix A, will be considered. The first is Gaussian:

$$F(u;\sigma) = \mathrm{e}^{-u^2/\sigma^2}, \tag{4.14}$$

and corresponds to a Gaussian illumination of the transmitting aperture. The second is produced by a uniformly illuminated circular aperture:

$$F(u;\sigma) = \frac{2J_1(u/\sigma)}{(u/\sigma)}. \tag{4.15}$$

Using (3.16) we have

$$u^2 = x^{*2} + y^{*2} = Ax^2 + Bx(y - y_0) + Cxz + D(y - y_0)^2 + E(y - y_0)z + Fz^2, \tag{4.16}$$

in which

$$\left.\begin{array}{lll} A = \cos^2\alpha_{\mathrm{t}}, & B = \sin 2\alpha_{\mathrm{t}} \sin\beta_{\mathrm{t}}, & C = -\cos\beta_{\mathrm{t}} \sin 2\alpha_{\mathrm{t}}, \\ D = \cos^2\beta_{\mathrm{t}} + \sin^2\alpha_{\mathrm{t}} \sin^2\beta_{\mathrm{t}}, & E = \cos^2\alpha_{\mathrm{t}} \sin 2\beta_{\mathrm{t}}, & F = \cos^2\beta_{\mathrm{t}} \sin^2\alpha_{\mathrm{t}} + \sin^2\beta_{\mathrm{t}}. \end{array}\right\} \tag{4.17}$$

Keeping all the terms in (4.16) makes the resulting integrals analytically intractable. Thus we make the fourth approximation that the beam is much wider than the cross-sectional (y, z) dimensions of the wake. In the wide beam limit, the beam amplitude

varies only along the axis of the wake and is constant within each cross-section of the wake. Thus setting $y = z = 0$ in (4.16) we obtain:

$$u^2 \approx x^{*2} + y^{*2} = Ax^2 - Bxy_0 + Dy_0^2. \tag{4.18}$$

To calculate the scattered power flux we need the scattered magnetic field corresponding to (4.2). Using the Maxwell equation

$$\boldsymbol{H}_\mathrm{s} = \frac{1}{\mathrm{i}\omega\mu_0}\nabla \times \boldsymbol{E}_\mathrm{s}, \tag{4.19}$$

we obtain to leading order in the far field

$$\boldsymbol{H}_\mathrm{s}^* = \frac{k}{R_\mathrm{r}\omega\mu_0}\mathrm{e}^{-\mathrm{i}kR_\mathrm{r}}(\hat{\boldsymbol{o}} \times \boldsymbol{f})^*. \tag{4.20}$$

Substituting (4.20) into (3.12) and noting that according to (4.8) $\boldsymbol{f}$ is of the form $\boldsymbol{f} = \boldsymbol{s}\mathscr{C}$ where $\boldsymbol{s}$ is a real vector perpendicular to $\hat{\boldsymbol{o}}$ and $\mathscr{C}$ is a complex number, we conclude that

$$\boldsymbol{S}_\mathrm{s}(\boldsymbol{x}) = \frac{k}{2R_\mathrm{r}^2\omega\mu_0}|\boldsymbol{f}|^2\hat{\boldsymbol{o}}. \tag{4.21}$$

The incident flux in the definition of the radar cross-section (1.2) is taken to be that for the original conical beam, namely, $c\varepsilon_0/2$. Hence (1.2) gives simply

$$\mathrm{RCS} = 4\pi|\boldsymbol{f}|^2. \tag{4.22}$$

4.2. *Scattering off a Fourier mode*

Begin by Fourier decomposing the dielectric constant in the axial and azimuthal directions:

$$\Delta\varepsilon_\mathrm{r}(\boldsymbol{x}) = \sum_{k_x,m} \Delta\hat{\varepsilon}_\mathrm{r}(r; k_x, m)\,\mathrm{e}^{\mathrm{i}(k_x x + m\phi)}. \tag{4.23}$$

To justify the sum in k_x instead of an integral, assume that there is a periodicity length L_x and then let $L_x \to \infty$.

Substituting the Fourier expansion (4.23) and the Gaussian incident beam (4.14) into (4.8) gives

$$\boldsymbol{f} = \sum_{k_x,m} \hat{\boldsymbol{f}}(k_x, m), \tag{4.24}$$

where

$$\hat{\boldsymbol{f}}(k_x, m) = \frac{\boldsymbol{s}k^2\mathrm{e}^{\mathrm{i}k\Phi}}{4\pi} I_x \int_0^\infty r\mathrm{d}r\Delta\hat{\varepsilon}_\mathrm{r}(r; k_x, m) I_\phi(r), \tag{4.25}$$

and I_ϕ and I_x are the following integrals (for a Gaussian beam):

$$I_\phi = \int_0^{2\pi} \mathrm{d}\phi\,\mathrm{e}^{-\mathrm{i}kr(S\cos\phi + Q\sin\phi)}\,\mathrm{e}^{\mathrm{i}m\phi} \tag{4.26}$$

$$= 2\mathrm{e}^{\mathrm{i}m\phi_1}\mathrm{i}^m\pi J_m(-\tilde{k}r), \tag{4.27}$$

$$I_x = \mathrm{e}^{-Dy_0^2/\sigma^2}\int_{-\infty}^{\infty} \mathrm{d}x \exp(-(Ax^2 - Bxy_0)/\sigma^2)\exp(-\mathrm{i}x(kP - k_x)) \tag{4.28}$$

$$= \frac{\pi^{1/2}\sigma}{A^{1/2}}\exp((y_0/\sigma)^2[B^2/(4A) - D])\exp(-\mathrm{i}k'By_0/(2A))\exp(-(k'\sigma)^2/(4A)). \tag{4.29}$$

The integral with respect to ϕ was obtained by letting $kQ = \tilde{k}\sin\phi_1$, $kS = \tilde{k}\cos\phi_1$, so that $\tilde{k} = k(S^2 + Q^2)^{1/2}$ and using an integral tabulated in Gradshteyn & Ryzhik (1980, p. 482).

The integral I_x was obtained by letting $k' = kP - k_x$ and completing the square on the exponent. Note that I_x has a Gaussian cut-off factor if the beam is off-centre: $\exp\{[B^2/(4A) - D](y_0/\sigma)^2\}$, where the argument can be shown to be negative definite. This corresponds to the 'blip' as the radar scans across the vortex. We shall henceforth set $y_0 = 0$. I_x also has a cut-off due to finite beam size as represented by the factor $\exp(-(k'\sigma)^2/(4A))$ ($k' \equiv kP - k_x$). It implies that the contribution to the radar cross-section versus frequency by a fluctuation in refractive index at wavenumber k_x is a 'bump' centred at radio wavenumber $k = k_x/P$ which has a half-width of $\delta k = 2A^{1/2}/(P\sigma)$. This result is analogous to the Bragg condition of Tatarski (1961). The cut-off is eliminated when it has infinite width, i.e. when $P \equiv \sin\alpha_r + \sin\alpha_t = 0$. This holds if the receiver is at the direction of specular reflection ($\alpha_r = -\alpha_t$). Note that for backscattering ($\alpha_r = \alpha_t$), perfectly normal incidence ($\alpha_r = \alpha_t = 0$) is required to eliminate the cut-off. The cut-off is also eliminated if $\alpha_r = \alpha_t \pm \pi$ and it corresponds to the receiver being on the other side of the transmitter relative to the wake axis.

For the Bessel function beam the analysis is very similar; only the integral I_x is different:

$$I_x = \int_{-\infty}^{\infty} \mathrm{d}x \frac{2J_1(u/\sigma)}{u/\sigma} \mathrm{e}^{-\mathrm{i}k'x} = \frac{4\sigma}{A} \begin{cases} [1 - (k'\sigma)^2/A]^{1/2} & 0 \leqslant k'\sigma/A^{1/2} < 1, \\ 0 & k'\sigma/A^{1/2} \geqslant 1, \end{cases} \tag{4.30}$$

where $u = (Ax^2)^{1/2}$. In deriving (4.30) the beam offset y_0 was set to zero for analytical tractability. Thus one sees that the Gaussian cut-off for the Gaussian beam has been replaced by a sharp cut-off and the same conditions hold for the elimination of this cut-off.

4.3. *Approximate scattering by mechanisms A and B*

To obtain RCS $= 4\pi|\boldsymbol{f}|^2$ for mechanisms A and B set $k_x = m = 0$. Then the only quantity that distinguishes the two mechanisms is the radial integral I_r in (4.25) which we now seek to obtain.

4.3.1. *Mechanism A: radial density gradient in a vortex core*

For the purpose of the approximate analysis, the numerically obtained variations of dielectric constant shown in figure 1 were fit to the following form:

$$\Delta\varepsilon_r(r) = \frac{\Delta\varepsilon_r^0}{(\eta/\eta_\varepsilon)^2 + 1}. \tag{4.31}$$

Here $\eta \equiv r/b_0$ and the parameter η_ε was chosen to make the fit agree with the actual curves at the half-amplitude point. The resulting fits were excellent through most of the core but for very large radii the actual decay was faster than represented by the fit.

For the fit (4.31) the radial integral in (4.25) is

$$I_r = (\eta_\varepsilon b_0)^2 \Delta\varepsilon_r^0 \int_0^{\infty} \frac{r\mathrm{d}r\, J_0(\tilde{k}r)}{r^2 + (b_0\eta_\varepsilon)^2} = (\eta_\varepsilon b_0)^2 \Delta\varepsilon_r^0 K_0(\tilde{k}b_0\eta_\varepsilon), \tag{4.32}$$

using Gradshteyn & Ryzhik (1980, 6.532.4). Owing to the exponential decay of K_0, the radial integral introduces a cut-off due to finite vortex core radius. The reader may wish to see this cut-off plotted in figure 3 in § 5.

This cut-off is eliminated as $\tilde{k} = k(S^2 + Q^2)^{1/2} \to 0$. This limit is realized in three cases: (i) when incident and scattering directions are along the vortex; (ii) when $\alpha_t = \alpha_r$ and $\beta_r = \beta_t + \pi$; (iii) for forward scattering ($\alpha_r = -\alpha_t$, $\beta_r = \beta_t + \pi$); with this condition on α_r and α_t, the beamwidth cut-off in the x-integral is also eliminated and therefore the forward direction has the greatest scattering.

It should be noted that I_r has a log divergence as $\tilde{k} \to 0$. This is a manifestation of the algebraic decay of the $\Delta\varepsilon_r(r)$ fit for large r. With a better representation of the large-r behaviour, the cut-off is eliminated without a singularity.

4.3.2. *Mechanism B: oval surrounding the vortex pair*

As mentioned in § 2.2.1 the oval can be approximated as a cylinder of radius a with a constant refractive index inside the cylinder and zero outside. In this case the radial integral in (4.25) is

$$\Delta\varepsilon_r^0 \int_0^a r \, \mathrm{d}r \, J_0(\tilde{k}r) = \frac{a\Delta\varepsilon_r^0}{\tilde{k}} J_1(\tilde{k}a). \tag{4.33}$$

5. Numerical results

5.1. *Mechanism A: radial density gradient in a vortex*

Here we consider the RCS due to a density gradient in a vortex arising from a balance of radial pressure gradient and centrifugal forces. The corresponding variation of dielectric constant was plotted in figure 1. Since the effect of humidity on $\Delta\varepsilon_r(r)$ was seen to be weak, attention is restricted to a dry atmosphere. We used the velocity profile of Spalart due to its better representation of the inner core. Then the appropriate curve in figure 1 is the dotted one without symbols. The results of the Born analysis were obtained using method A (§ 3.5).

A Gaussian beam having an e^{-1} half-width of $\theta_b = 1.5°$, a target range of 1 km and polarization angle of $\gamma = 0$ were chosen for illustrative purposes (the value of γ was found to be immaterial for backscattering).

Figure 3(a) plots the radar cross-section for various incident and scattering directions: the two cases of most practical relevance are backscattering at normal (– – – –,○) and off-normal (— · —,□) incidence. The results of the approximate analysis (lines) agree quite well with those of the Born analysis (symbols) even though the far-field parameter becomes $O(1)$ (figure 3b). The general features of the results are in accord with the discussion in § 4.3.1: one observes (i) a low-frequency cut-off for backscattering away from normal incidence (chain-dashed), (ii) a higher frequency cut-off at the scale of the vortex for backscattering at normal incidence (dashed) and specular reflection (not shown for clarity), (iii) elimination of both cut-offs for forward scattering (△). Finally, one observes (long-dashed, ▽) that some increase in frequency and reflectivity can be obtained even somewhat away from the forward direction, in particular when the transmitter and receiver are both looking up at the vortex with an elevation of 30°.

The limit frequency for the Born approximation is obtained by setting $L_s = \max(u_b, \delta_\varepsilon)$ in (3.10). The result is $f \ll 0.74$ GHz. This fails to be satisfied for the rightmost portion of the figure. From the Mie result for scattering by a sphere we expect that if the Born approximation were not made, the main difference would be that the forward scattering result, which increases linearly, would begin to oscillate and decrease in average slope as the weak scattering approximation began to be violated. We expect that the other results would continue to hold.

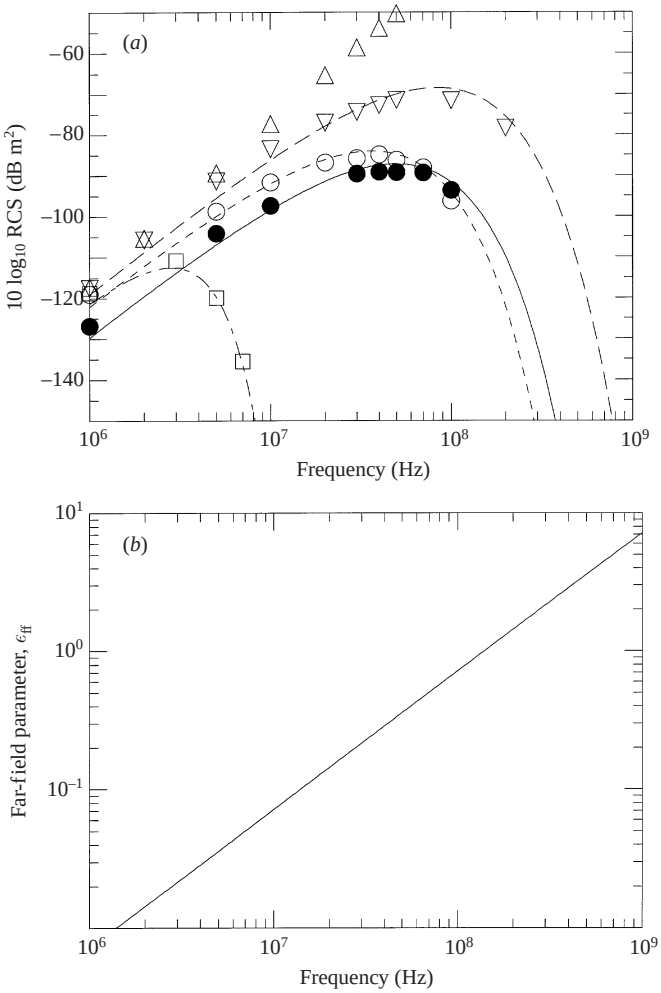

FIGURE 3. (*a*) Radar cross-section for a vortex due to a Gaussian beam at a range of 1 km. Unless indicated the results are for a heavy aircraft. The symbols correspond to the Born analysis and lines to the approximate analysis. —·—,□, backscattering away from normal incidence ($\alpha_t = \alpha_r = 30°$, $\beta_t = \beta_r = 0$); – – – –,○, backscattering at normal incidence ($\alpha_t = \alpha_r = 0°$, $\beta_t = \beta_r = 0$); – – –,▽, nearly forward scattering with 60° offset in β ($\alpha_t = -\alpha_r = 30°$, $\beta_t = 0$, $\beta_r = 120°$); △, forward scattering ($\alpha_t = -\alpha_r = 30°$, $\beta_t = 0$, $\beta_r = 180°$); ——,●, DC-8, backscattering at normal incidence. (*b*) Far-field parameter ϵ_{ff} for (*a*).

To emphasize differences between the Born and approximate analysis the range was varied beyond 1 km. For a point target the radar cross-section should be independent of range but not so for an extended target. For very short ranges the vortex will fill the beam and we expect the RCS to increase quadratically with range. When the range is large enough that the vortex spans the beam in only one direction, we expect the radar cross-section to increase linearly with range. To verify this, the frequency was kept fixed near the peak for normal-incidence backscattering ($f = 5 \times 10^7$ Hz) and the range was varied (see circles in figure 4*a*). It is interesting to note that the dependence on range according to the approximate analysis (dashed line) is quadratic, that is, as if the target were always beam filling in both directions. Figure 4(*b*) shows that the approximate analysis begins to show deviations from the Born analysis when the far-field parameter becomes greater than unity.

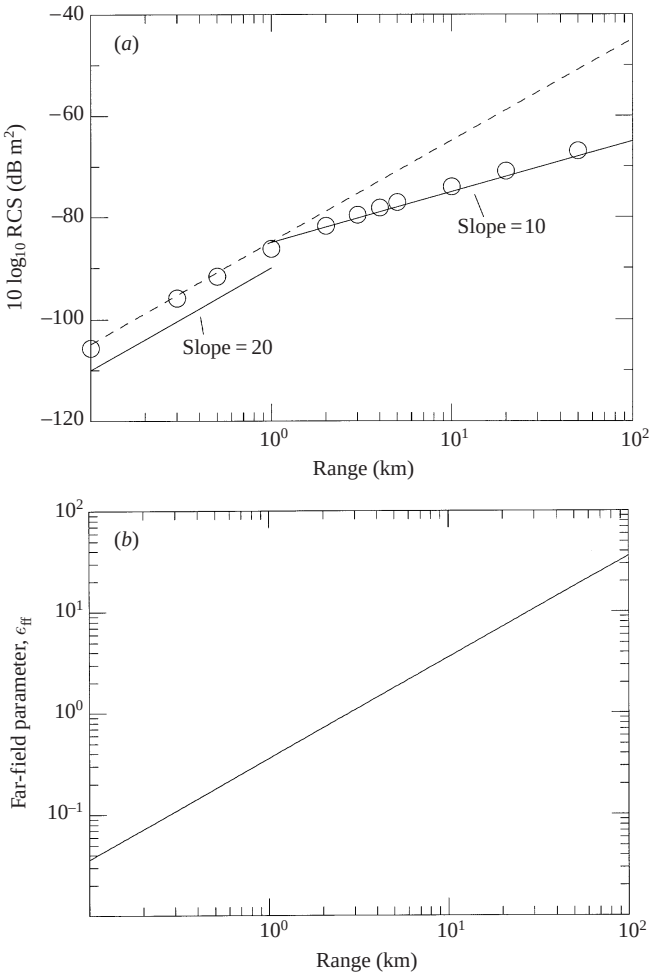

FIGURE 4. (*a*) Range dependence of vortex RCS for backscattering at normal incidence ($f = 5 \times 10^7$ Hz). O, Born analysis; – – – –, approximate analysis; ——, slope lines. (*b*) Far-field parameter, ϵ_{ff} for (*a*).

5.2. *Mechanism B: scattering by the oval*

This subsection has two parts. In the first, RCS of the oval is calculated for the parameters of the Kwajalein experiment and the results compared with measurements. In the second the range and frequency dependence of the RCS and errors introduced by various assumptions in the approximate analysis are studied.

5.2.1. *Comparison with experiment* (*Gilson 1992*)

We expect that at the high frequencies (> 50 MHz) of the Kwajalein experiment, the vortices themselves are ineffectual scatterers. Indeed, for the VHF radar at Kwajalein we calculated RCS = −86.8 for a vortex of a heavy aircraft in approach configuration at the experimental value of the range (the RCS for the cruising C-5A would be even lower due to its smaller circulation). This is 17 dB less than the measured values and therefore in attempting to predict the experimentally measured RCS we focus entirely on mechanism B.

Band	$\Delta\theta$ (mrad)	θ_b (deg.)	f_0 (GHz)	f_{lim} (GHz)	Waveform ID	Pulse width, τ (μs)	FM spread, Δf_{FM} (MHz)
VHF	48.8	2.37	0.162	0.084	V.25C	0.25	0
UHF	19.2	0.934	0.422	0.21	U.1C	0.10	0
L	10.6	0.516	1.32	0.39	L2	2	20
S	5.2	0.253	2.95	0.79	S3	3	60
C	5.2	0.253	5.67	0.79	NB	10.2	6
K_a	0.76	0.037	35.0	1.0	N2	50	12

TABLE 2. Radar parameters for the Kwajalein experiment. $\Delta\theta$: half-power beamwidth; θ_b: e^{-1} half-width of a corresponding Gaussian beam; f_0: carrier frequency; f_{lim}: limit frequency for validity of the Born approximation.

Experimental procedures and parameters (Gilson 1992; Roth *et al.* 1989) are now discussed:

(i) As discussed in § 2.2.2 we chose to simulate run 15 of the experiment at about 66 s after aircraft passage, the first instant when all radars in the experiment have detected the wake. The range of the target was 15 km and the radar was pointed normal to the wake.

(ii) Gilson (1992) plots RCS divided by a certain length and it is not possible to infer the raw RCS from his report. Fortunately, Dr Gilson kindly provided us with raw data.

(iii) All the radars in the experiment transmit a right circularly polarized wave and receive both right and left circularly polarized waves. So far our analysis has been for linear polarization. However, a circularly polarized wave is simply a superposition of two linearly polarized waves:

$$\boldsymbol{E}(\boldsymbol{x}) = E(\boldsymbol{x})(\hat{\boldsymbol{e}}_1 \pm \mathrm{i}\hat{\boldsymbol{e}}_2), \tag{5.1}$$

$$\boldsymbol{H}(\boldsymbol{x}) = H(\boldsymbol{x})(\mathrm{i}\hat{\boldsymbol{e}}_2 \pm \hat{\boldsymbol{e}}_1), \tag{5.2}$$

where $\hat{\boldsymbol{e}}_1 \perp \hat{\boldsymbol{e}}_2$ and the choice of plus signs gives a right circularly polarized wave and minus signs a left one. Further, note that a circularly polarized wave has simply twice the power flux of each of its linearly polarized components. If the incident beam has the form (5.1)–(5.2) then the linearly polarized analysis can be done separately for each component and the resulting scattered fields added. In this manner, it was verified from the numerical result that for all the cases presented here, the resulting scattered wave is also circularly polarized with the same helicity as the incident wave (the approximate analysis gives the same result). Thus both incident and scattered powers are doubled compared to the linearly polarized analysis and the RCS is unchanged.

(iv) The experiment used a pulsed radar whereas our analysis so far has been for a time-harmonic wave. Appendix B describes the treatment of a pulse and table 2 gives the characteristics of the pulse waveforms.

Figure 5 shows that the results of the Born analysis (●) and measured (○) RCS values have differences of between 2 and 13 dB while the approximate analysis (■) considerably overpredicts the RCS. We considered the possibility that part of the error in the Born analysis may be accounted for by the presence of internal structure within the oval. The first source of this to come into play (for a laminar oval) is that the lower stagnation point on the oval boundary is kinematically unstable. Any slight

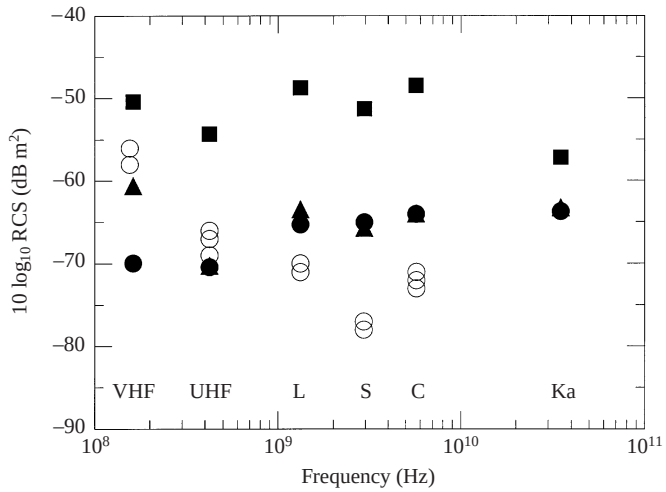

FIGURE 5. Comparison with experiment: ○, experimental data at about 66 s after passage of the airplane; ●, Born analysis for oval; ▲, Born analysis for oval with a slice of entrained fluid. ■, approximate analysis for oval.

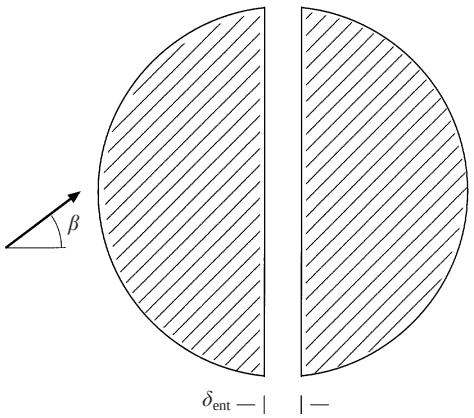

FIGURE 6. Model for the oval with a slice of entrained ambient fluid.

unsteadiness in the flow will cause a sliver of ambient fluid to be entrained into the oval along its centreplane (Rom-Kedar, Leonard & Wiggins 1990). A corresponding thin slice of oval fluid will be detrained from the top stagnation point. Both will produce additional surfaces of reflection. To gauge the importance of this we calculated the reflectivity of an oval with a slice of ambient fluid (figure 6). Using the elevation angle for the experiment ($\beta = 5.8$) we obtain the ▲ in figure 5. There is an improvement only at the VHF frequency. This is because the pulses reflected from the slice add to the two pulses reflected from the outer boundary of the oval as shown in figure 7. For the other frequency cases, all three reflection pulses remain distinct, causing no change in the peak RCS. The width of the slice used in this calculation was $\delta_{\text{ent}} = 0.10a$. A thinner slice ($\delta_{\text{ent}} = 0.02a$) was also tried and it produced small RCS changes ($\leqslant -1.5$ dB) compared to the thicker slice. This suggests that the presence of an internal boundary is more important than its precise form.

The Born analysis gives a rapid cut-off away from normal incidence. On the other hand, comparing experiments at 45° and 90° incidence (Gilson's runs 1 and

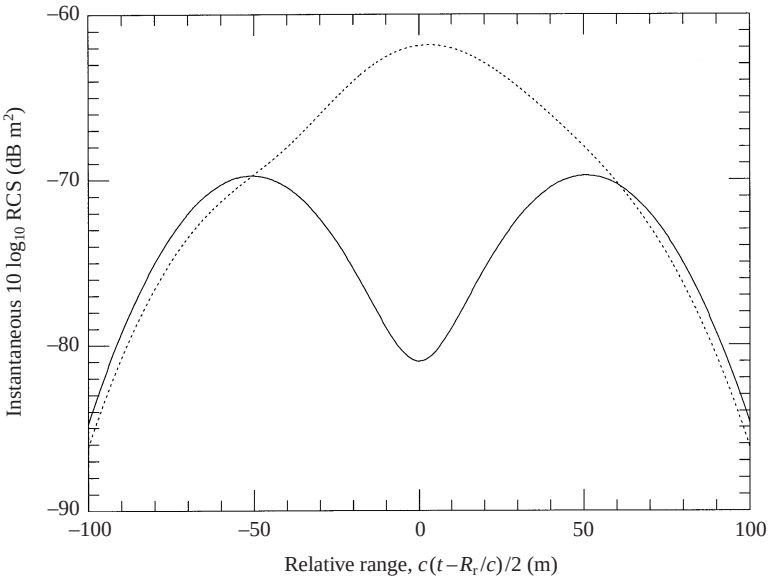

FIGURE 7. Returned pulse envelope calculated for Gilson's (1992) VHF case. The abscissa is time expressed as a range, $c(t - R_r/c)/2$; the division by 2 converts from round-trip travel distance between scattering centres to one-way distance. ——, Oval; ·····, Oval with slice of entrained ambient fluid.

17, respectively) does not reveal significant differences. Moreover, the experiments searched for a flash at normal incidence and found none. We estimate in § 6.2 that the boundary of the oval is very likely to be turbulent and suggest that this may account for the lack of directional dependence in the experiment. There we will also estimate the attenuation due to the turbulent boundary and show that it is consistent with the experimental observation of a cut-off somewhere between 5.67 GHz and 35 GHz.

How valid is use of the Born approximation for the Kwajalein experiment? An upper frequency limit f_{lim} for validity of the Born approximation was defined using (3.10) by replacing the inequality with an equality and using

$$L_s = \max(R_t \sin\theta_b, a) \tag{5.3}$$

for the characteristic size of the scattering region. Table 2 provides values of f_{lim} for each experimental case. They show that in the experiment frequencies are between factors of 2 and 6 higher than f_{lim}. Therefore in the future it would be worthwhile to perform a scattering analysis that does not invoke the Born approximation. A possible approach for such an analysis might be geometric optics which is valid for large frequencies ($ka \ll 1$) but arbitrary $\Delta\varepsilon_r$.

5.2.2. *Test of various approximations*

The goal of this subsection is to present a study of the errors introduced by various assumptions in the approximate analysis. This is done by introducing (in various combinations) assumptions of the approximate analysis into the computer code (method B) for the Born analysis. Let us recall that starting from the Born analysis, the approximate analysis is obtained by: (i) replacing the Green's function with its far-field version; (ii) replacing the conical incident beam with a cylindrical beam; (iii) assuming that the beam is much wider than the size of the oval's cross-section.

Range dependence. In the first test, the parameters chosen were those of the Kwajalein S-band test and the range was varied. The results, which are shown figure 8,

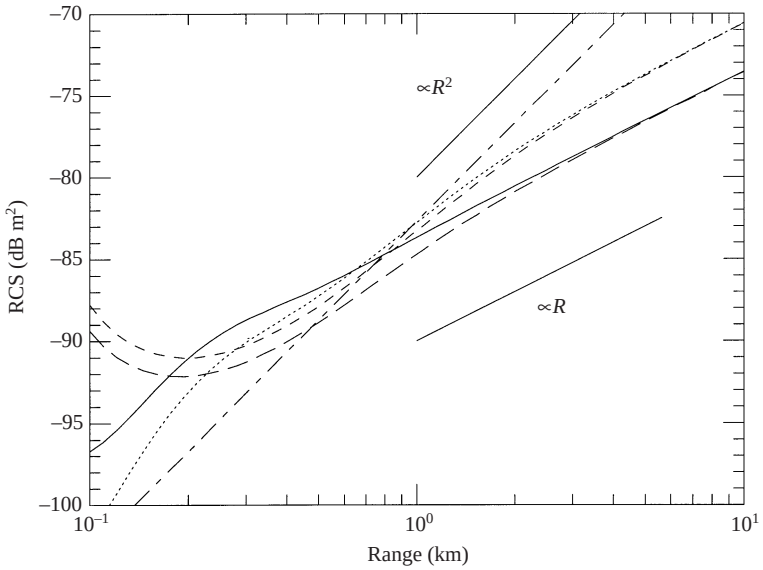

FIGURE 8. Range dependence of oval RCS for various approximations. ——, Born analysis; ·····, far-field Green's function only; – – – –, wide cylindrical beam only; — - —, both far-field and wide cylindrical beam; — — — —, wide cylindrical beam approximation but without assumption (d) in Appendix A, § A.2. Reference lines for linear and quadratic dependence are also shown.

are for a time-harmonic wave. The Born analysis (solid line) gives R^2 behaviour for small ranges, characteristic of a beam filling target, followed by the linear behaviour characteristic of a target that fills the beam in only one direction. Replacing the Green's function with the far-field G gives the dotted line, which overpredicts the RCS by a constant number of dB as the range increases. Using the full Green's function but replacing the conical beam with a cylindrical beam and invoking the wide beam approximation gives a result (dashed curve) that agrees surprisingly well with the far-field G result for large ranges. This is partially understandable since one of the cylindrical beam approximations also requires smallness of a far-field parameter in order to be valid; this is approximation (d) in Appendix A, § A.2 which replaces spherical with plane wavefronts. If we drop assumption (d), then the result (long-dashed) agrees with the Born analysis as the range increases. When both the far-field G and cylindrical beam are used, the result (chain-dashed) gives an R^2 behaviour throughout which is erroneous for large R. This curve agrees (as it should) with the analytical result of the approximate analysis (not shown for clarity) and thus provides a check on the accuracy of the quadratures for method B.

Frequency dependence. Figure 9 shows the frequency dependence for a time-harmonic incident wave. Besides the frequency, the rest of the parameters are those for the Kwajalein VHF case. The Born analysis (solid line) gives a flat frequency dependence. The curve is punctuated by regular oscillations having a width $\Delta f = c/(4a)$ due to interference between the two effective scattering centres of the target (see Appendix B); the fluctuations appear irregular due to a coarse number of plot points. Using the far-field G produces the dotted curve which only slightly over-predicts the RCS. The curve for the wide cylindrical beam (full G) is very close to the dotted curve and is not shown for clarity. However, when both far-field G and wide cylindrical beam are invoked (to yield the approximate analysis) the result (long-dashed curve) has an erroneous RCS $\propto k$ behaviour.

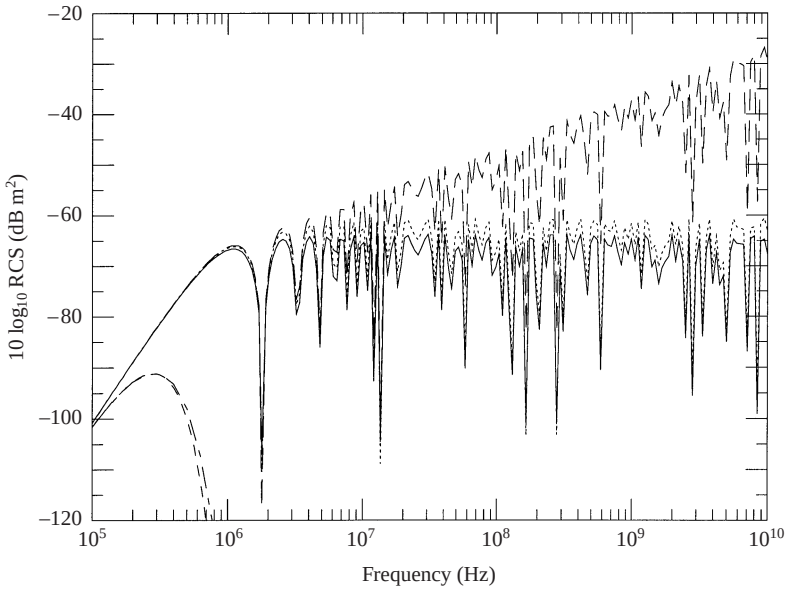

FIGURE 9. Frequency dependence of oval RCS. ——, Born analysis, normal incidence; — — —, approximate analysis, normal incidence; · · · · · ·, far-field G, normal incidence; — - —, Born analysis, 15° off-normal incidence; – – –, approximate analysis, 15° off-normal incidence.

6. Qualitative assessment of effects not present in the two-dimensional picture

In this section various phenomena not included in the two-dimensional picture are discussed and their qualitative effect on radar cross-section suggested. Most of the phenomena are well-known. Two new aspects are: (i) a study of the effect of rotating shear on the elliptic flow instability; (ii) an estimate indicating that the baroclinically generated shear layer at the oval boundary is turbulent.

6.1. *Phenomena affecting mechanism A*

6.1.1. *Core waviness*

Vortex core waviness in the form of Crow (1970) and Widnall (Thomas & Auerbach 1994; Leweke & Williamson 1998) instabilities may arise from small disturbances or from forcing by atmospheric turbulence (Spalart & Wray 1996; Risso, Corjon & Stoessel 1997). Both instabilities have wavelengths so large that they are irrelevant as a mechanism for scattering above about 20 MHz. However, they would cause the axial mean of the refractive index to be smeared out in r. A beam that is wider than the wavelength of the Crow instability (≈ 400 m for a heavy airplane) would be sensitive to this axial mean and therefore reflectivity would diminish in strength and shift to frequencies lower than 50 MHz. Tighter beams (larger antenna arrays) would be required to mitigate this effect.

6.1.2. *Turbulence suppression within vortex cores*

This subsection justifies the neglect of turbulence within the vortex cores. Rotation has profound effects on turbulence which most turbulence models are unable to capture. First, the rate of energy transfer and hence dissipation is reduced (e.g. Bardina, Ferziger & Rogallo 1985) because rotation scrambles nonlinear interactions. A more important effect is the drastic alteration of turbulence production. There are

three mean velocity gradients which can act as turbulence production mechanisms within the vortex:

(i) There is a jet/wake flow along the vortex axis but this decays quite rapidly behind the wing.

(ii) The circumferential velocity around the axis leads to shearing of fluid elements as they rotate. The Bradshaw criterion for stability of shear in a rotating frame when applied to a vortex with single-sign vorticity predicts that the flow is locally stable at each r (e.g. LeBlanc & Cambon 1997). Indeed Qin (1998) found via direct numerical simulation that there is *negative* production of turbulent kinetic energy within vortex cores.

(iii) Finally, the only remaining mechanism for turbulence production is the strain induced by one vortex upon the other. It is responsible for the Crow and Widnall instabilities discussed earlier and the ultra-short-wave elliptic flow instability (e.g. Landman & Saffman 1987). The question arises of whether the elliptic instability can be excited in the presence of the stabilizing effect of rotating shear. To address this question without undertaking a full stability analysis of a vortex pair, we perform an analysis which accounts for only the local velocity gradient. This is valid for waves much smaller than the vortex core size. The local velocity gradient (following a fluid element in an inertial frame) has three parts: rotation, strain induced by the other vortex and rotating shear. The first two alone lead to the elliptic instability. To this we add shear (of rate S) rotating at angular velocity Ω. The velocity gradient matrix then becomes

$$\boldsymbol{A} = \begin{pmatrix} 0 & -\bar{\gamma} - e & 0 \\ \bar{\gamma} - e & 0 & 0 \\ 0 & 0 & 0 \end{pmatrix} + S \begin{pmatrix} -\sin \Omega t \cos \Omega t & \cos^2 \Omega t & 0 \\ -\sin^2 \Omega t & \sin \Omega t \cos \Omega t & 0 \\ 0 & 0 & 0 \end{pmatrix}. \tag{6.1}$$

The value of Ω was chosen to be the rate of rotation of fluid particles in the elliptic flow, i.e. $\Omega = (\bar{\gamma}^2 - \epsilon^2)^{1/2}$. Had Ω been chosen to be the rate of rotation, $\bar{\gamma}$, of fluid particles without the strain then the shear axes would move ahead of the axes of a fluid element which is not physical. For an axisymmetric circumferential flow $u_\theta(r)$ we have

$$\bar{\gamma} = \frac{u_\theta}{r} \quad \text{and} \quad S = -\left(\frac{\partial u_\theta}{\partial r} - \frac{u_\theta}{r} \right). \tag{6.2}$$

The strain rate due to the other member of a vortex pair is

$$e = 2 \times \frac{\Gamma}{2\pi b_0^2}, \tag{6.3}$$

where the induced strain has been multiplied by 2 in order that the growth rate and ellipticity of the elliptic streamline flow match that of a vortex of uniform vorticity surrounded by potential flow. The evolution of a single mode was considered at several values of r/δ_L inside a Lamb–Oseen vortex with a value of $\delta_L/b_0 = 0.088$ given by Rennich (1997) for a large aircraft in approach. The modes investigated were those known to be the most unstable for the elliptic streamline flow. These modes have wavevector lying in a cone at 60° relative to the vortex axis. Within this cone the initial azimuthal angle φ is free. Figure 10 shows the amplification factor of the velocity perturbation during the time that the vortex pair descends five vortex spacings. The different curves are for different locations, r/δ, within the core. At the centre of the core (chain dashed line) there is no shear and the elliptic instability is active for all φ. As one moves outward, the shear stabilizes all modes except

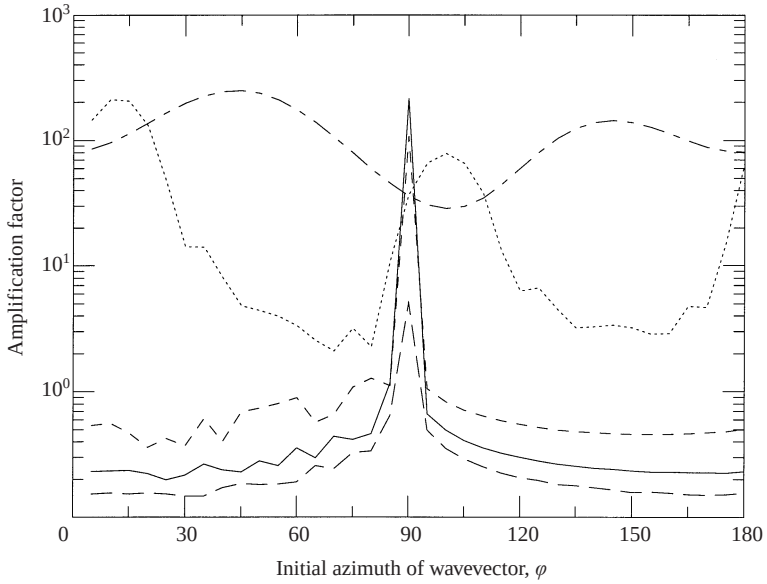

FIGURE 10. Amplification factor of disturbances at various locations in a Lamb–Oseen vortex subject to strain by another vortex. —·—, $r/\delta_L = 0.0$; ·····, $r/\delta_L = 0.01$; – – – –, $r/\delta_L = 0.10$; ——, $r/\delta_L = 0.20$; — — —, $r/\delta_L = 0.30$.

those located in a thin band near $\varphi = 90°$. This wavevector direction corresponds to wavefronts that are initially parallel to the shear flow and continue to rotate with it and therefore are never deformed by it. By $r/\delta = 0.3$ (long-dashed curve) the growth of even these waves is suppressed by the shear. We thus conclude that roughly only the inner 20% of the vortex core, or a diameter of 170 cm for a large airplane, is capable of supporting an elliptic instability, and even this produces amplification factors that are not significant.

6.2. *Phenomena affecting mechanism B*

6.2.1. *Turbulence within the boundary of the oval*

In the presence of stratification, baroclinic torque generates a shear layer at the boundary of the oval (Spalart 1996). Can this shear layer become turbulent? We attempt to answer this by making conservative estimates for growth rates of Kelvin–Helmholtz (KH) and centrifugal instabilities. The turbulent wing boundary layer, part of which ends up on the oval boundary as it rolls up, could provide the initial disturbances for these instabilities.

In the present situation the KH instability is complicated by the variation of vortex sheet strength $\tilde{\gamma}(s)$ and thickness $\delta(s)$ along the shear layer and by the fact that the lower half of the oval boundary experiences an extensional strain (which is stabilizing) and the upper half a compressive strain (which is destabilizing). To obtain the distribution of $\tilde{\gamma}(s,t)$ (as a function of position and time) we used the model of Crow (1974). We expect the thickness $\delta(s)$ of the layer to reach a steady state (dependent only upon position along the layer but not on time) in which newly diffused vorticity is swept away by the flow. To obtain $\delta(s)$ we begin very near the lower stagnation point where fluid elements are strained but not advected. Here the thickness of the layer is set by a balance of strain and diffusion. Starting with this thickness, we then advect a fluid particle along the oval boundary and

evolve its thickness according to the equations for a strained diffusion layer presented in Leonard, Rom-Kedar & Wiggins (1987). We note that the appropriate strain component to use in these equations is the one tangent to the boundary of the oval.

The growth rate of the KH instability in the absence of strain is proportional to $\tilde{\gamma}/\delta$ times a coefficient that increases with Reynolds number (Betchov & Szewczyk 1963). We find that both $\tilde{\gamma}(s,t)/\delta(s)$ and the Reynolds number increase monotonically along the layer from the lower stagnation point. To account for the effect of strain on the instability in the most conservative (erring towards stability) way possible, we set the growth rate to be zero in the stabilized lower half of the oval while for the upper half we used the value of the growth rate of an unstrained layer at the beginning of the upper half. We thus believe our estimate of growth rate provides a lower bound. Furthermore, since the KH instability is convective, the total growth must be computed for only that time interval during which a fluid element remains on the boundary, i.e. before it enters the wake of the oval. Since we were interested in turbulence in the boundary of the oval (rather than in the wake of the oval), to obtain the total growth we multiplied the growth rate by the time that a particle takes to travel from the beginning of the upper half to the point where the distance to the symmetry plane is halved.

Numerical values were inserted for the Kwajalein experiment (run 15) 22 s after passage of the aircraft. We find that there are 13 e-folds of the KH instability in the 26 s it takes for a particle to travel the distance specified in the previous paragraph. Thus we are confident that at the instant of the first measurement (66 s after aircraft passage) the upper surface of the oval is turbulent.

Since the vorticity in the oval boundary is of opposite sign to the vortices, we must also entertain the possibility of centrifugal instability. We estimated the growth rate to be the square root of the Rayleigh discriminant Φ_{R} where (e.g. Drazin & Reid 1981, p. 69)

$$\Phi_{\mathrm{R}} = 2|\boldsymbol{u}|\omega/r. \tag{6.4}$$

Here $|\boldsymbol{u}|$ is the velocity magnitude and $\omega \approx \tilde{\gamma}/\delta$ is the vorticity. The corresponding e-folding time is about 2 s along most of the oval boundary, which also suggests a turbulent boundary.

If we repeat the above exercise using the parameters of Spalart's (1996) two-dimensional simulation (taking his $N_0^* = 0.5$, non-dimensional time $t = 4$, and his $Re = 4 \times 10^4$) we find that even the inviscid growth rates of the KH instability are too weak; this is compounded by a very small Reynolds number based on shear layer strength and thickness. Thus we are not disturbed by the fact that his simulations do not show an instability.

6.2.2. *Scattering due to an oval boundary with arbitrary shape and thickness distribution*

The boundary of the oval will become convoluted due to turbulence. Potential flow fluctuations arising from vortex core waviness or co-rotation of flap vortices around wing-tip vortices will also cause the boundary to become stretched and folded into striations (e.g. Rom-Kedar *et al.* 1990; Spalart 1996). Owing to thermal diffusion, at each point along the boundary there will exist a layer across which the temperature will smoothly change from its ambient to its interior value. For small layer thickness compared to radius of curvature a locally one-dimensional model is valid. In particular, if η is the coordinate normal to the surface (positive into the

interior) then linearizing (2.1) and ignoring humidity:

$$\Delta\varepsilon_{\mathrm{r}}(\eta) = \Delta\varepsilon_{\mathrm{r}}^{0}\tfrac{1}{2}[1 + \mathrm{erf}(\eta/\delta)], \tag{6.5}$$

where the thickness δ will assume a different value on each point on the surface. This value depends on the local stretch and on interactions with adjacent layers (Leonard *et al.* 1987).

To evaluate the effect of a convoluted boundary on scattering consider an infinitesimally thin pencil of rays within the radar beam. The pencil will repeatedly enter and exit the interior region. We evaluate, using (4.8), the scattering amplitude $\mathrm{d}\boldsymbol{f}(\hat{\boldsymbol{o}}, \hat{\boldsymbol{i}})$ due to one entry and exit. The total scattering amplitude will be a sum over all entry–exit pairs and an integral over all pencils comprising the radar beam. The result (for backscattering) is

$$\mathrm{d}\boldsymbol{f} = \frac{\hat{\boldsymbol{x}}^{*}\mathrm{i}k\mathrm{e}^{\mathrm{i}kz_0^{*}}}{8\pi}F(x^{*}, y^{*})\,\mathrm{d}x^{*}\,\mathrm{d}y^{*}\Delta\varepsilon_{\mathrm{r}}^{0}[\exp(-\mathrm{i}kL)\exp(-(k\delta_i/\sin\psi_i)^2) - \exp(\mathrm{i}kL)\exp(-(k\delta_o/\sin\psi_o)^2)]. \tag{6.6}$$

Here (x^{*}, y^{*}, z^{*}) are beam coordinates, z^{*} being along the pencil and (x^{*}, y^{*}) normal to the pencil. The magnitude of the incident electric field in the pencil is $F(x^{*}, y^{*})$ and its direction is along $\hat{\boldsymbol{x}}^{*}$. Between the entry and exit, the length of the pencil is L and its midpoint is at z_0^{*}. The width of the error function layers at entry and exit are δ_i and δ_o (i.e. delta in and delta out), respectively. Similarly the angle of the pencil relative to the tangent plane of the layers is ψ_i and ψ_o.

Note from (6.6) that the pencil need not have normal incidence to the layers for reflection to occur. In the case of the two-dimensional targets, normal incidence is a requirement for backscattering because for every reflected pencil there is another which cancels it. In the case of the convoluted surface, such a cancellation becomes unlikely. Stated more positively in terms of the Bragg condition: it is very likely that there will be a non-zero Fourier mode with wavevector parallel to the beam.

Combining the arguments of the last two subsections, we are led to believe that turbulence in the boundary of the oval is a plausible explanation for Gilson's observed lack of directional dependence.

6.2.3. *High-frequency cut-off in RCS*

The Kwajalein tests observed reflectivity up to 5.66 GHz but not at 35 GHz. The frequency where the cut-off in reflectivity occurs is determined by the smallest scale at which gradients in refractive index exist.

Let us first estimate the cut-off for laminar flow. In § 6.2.1 we described how the velocity thickness of the oval boundary can be calculated. The calculation of temperature thickness δ_T merely replaces viscosity with diffusivity κ. According to equation (6.6) the cut-off length scale δ_{c} will be the minimum value of $\delta_{\mathrm{diff}}/\sin\psi$ along the boundary and the corresponding attenuation factor is $\exp(-k^2\delta_{\mathrm{c}}^2)$. Using the elevation angle $\beta = 5.8^{\circ}$ of the Kwajalein experiment we find $\delta_{\mathrm{c}} = 2.78$ cm. Figure 11 (dotted line) shows that the corresponding attenuation factor is too strong to account for the experimental observations.

It is difficult to estimate the smallest scale when the flow is turbulent; however, we may calculate the next smaller scale in the KH instability. This is the thickness in the braid region between the KH rollers. First, we calculate the circulation in the KH vortices as $\Gamma_{\mathrm{KH}} = \tilde{\gamma}\lambda_{\mathrm{KH}}$ where λ_{KH} is the instability wavelength. From this the strain rate in the braid region due to two KH vortices can be calculated as

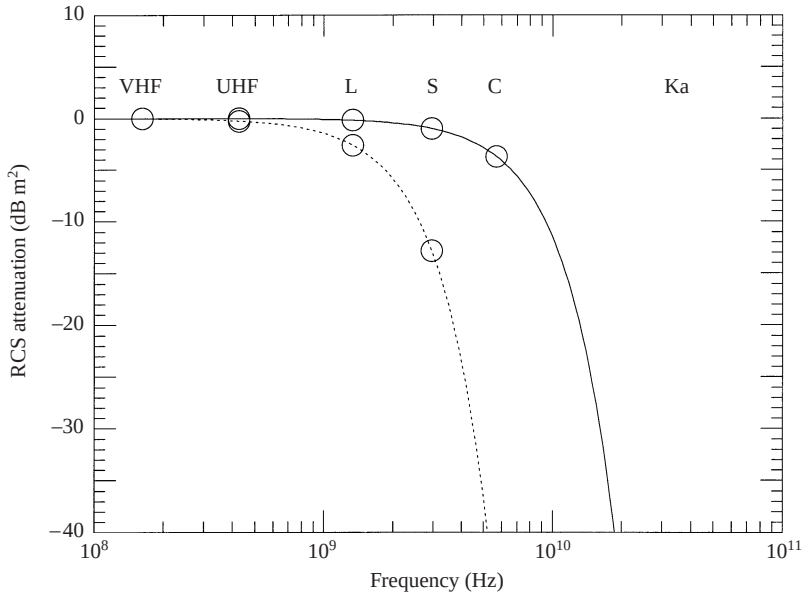

FIGURE 11. RCS attenuation due to the oval boundary. ——, $\delta_c = 0.55\,\text{cm}$; · · · · · ·, $\delta_c = 2.78\,\text{cm}$; O, frequencies corresponding to the Kwajalein experiment.

$e_{\text{braids}} = 2\Gamma_{\text{KH}}/[2\pi(\lambda_{\text{KH}}/2)^2]$. Finally, the thickness of the braids is obtained as $\delta_{\text{braids}} = (2\kappa/e_{\text{braids}})^{1/2}$. The minimum value of this quantity along the destabilized upper half of the oval in the Kwajalein experiment is 0.55 cm. The corresponding attenuation factor, shown in figure 11 as the solid line, is in accord with the observations: there is very little attenuation at 5.66 GHz but a lot at 35 GHz.

7. Practical recommendations

7.1. *Prospects for detection of the vortex cores*

No test so far has been at frequencies as low as 50 MHz where, according to the analysis, the density gradient in the vortex cores reflects (figure 3). Since this mechanism is independent of atmospheric conditions, it is worthwhile to discuss its potential use in air traffic control (ATC).

(i) It is fortunate that 50 MHz is where many radars operate around the world for atmospheric profiling. Such radars are called ST or MST (M: mesospheric, S: stratospheric, T: tropospheric) radars. Thus the predicted reflectivity could be tested.

(ii) Rain clutter is not a problem at this frequency, though clutter from clear-air turbulence might be.

(iii) Most ST radars are used for measurements in the high atmosphere but recently a restriction on minimum range (which arises due to ringing of the antenna system after a pulse is transmitted) has been partially overcome and a boundary layer profiler has been developed (Vincent *et al.* 1998). It has a height coverage of 400–3200 m. This radar achieves a range resolution of 150 m with a pulse width of 1 μs. The minimum range restriction may be eliminated by using separate transmit and receive antenna arrays (Dr H. McDonald of NASA Ames suggested this). The range resolution may be improved by using pulse compression techniques.

Range (km)	RCS	Half-power beam diameter (m)	Power (W)
0.4	−87.9	70	1.40
1	−83.9	175	21.7
2	−80.9	349	173
3	−79.1	524	586

TABLE 3. Power required to detect a vortex of a heavy aircraft at various ranges for the type of radar discussed in the text.

(iv) The transmitter power required for detection is

$$P_t = \frac{(4\pi)^3 R^4 N_p \times \mathrm{SNR}}{G_t G_r \lambda^2 L_{sys} \times \mathrm{RCS}}, \tag{7.1}$$

where $N_p = -185\,\mathrm{dB\ W}$ and $L_{sys} = -7\,\mathrm{dB}$ are the noise power and system loss for an ST radar (Kingsley & Quegan 1992, p. 199). $\mathrm{SNR} = 20\,\mathrm{dB}$ is the desired signal-to-noise ratio, $\lambda = 6\,\mathrm{m}$ is the wavelength. For an antenna array the half-power beamwidth (in degrees) broadside to the array is (Skolnik 1970, chap. 11, p. 2)

$$\Delta\theta_{1/2} \approx \frac{100}{\sqrt{N_{el}}}, \tag{7.2}$$

where N_{el} is the number of elements, and the gain on transmit and receive is $G_t = G_r \approx \pi N_{el}$. We consider a modest array of 10×10 elements spaced $\lambda/2 = 3\,\mathrm{m}$ apart. The corresponding half-power beamwidth is $\Delta\theta_{1/2} = 10^\circ$ which implies an e^{-1} half-width of a Gaussian beam of $\theta_b = 8.49^\circ$. Table 3 shows that the powers required to detect the vortex of a heavy aircraft at various ranges are quite modest. A smaller array size may be achievable by using individual elements (such as yagis) which are more directive than dipoles.

(v) ST radars have limited steering capability, usually just a few fixed beam directions. The ability to steer the beam by using phase differences among elements would have to be incorporated into such radars if they are to be used for ATC. Since it is unlikely that three-dimensional disturbances will exist in the vortex across a broad spectrum of wave angles, detection may be possible at only normal incidence.

(vi) Detection of the vortices at 50 MHz may also be combined with a RASS (Radio Acoustic Sounding System). The corresponding acoustic frequency is 114 KHz for which the attenuation is $1\,\mathrm{dB\,km^{-1}}$. This should be compared with the higher attenuation of $16\,\mathrm{dB\,km^{-1}}$ in the RASS system of Rubin (2000) which has the advantage of being smaller.

(vii) Finally let us note that the oval will also scatter at 50 MHz with the same strength as at higher frequencies (see figure 9).

The above estimates have ignored detection of aircraft vortices in landing configurations. This would have to be taken into account in a fully-fledged feasibility study.

7.2. *A note on the role of engine exhaust*

At approach, the exhaust of a heavy aircraft has a temperature of 477 K and each engine emits $1200–6000\,\mathrm{lb\,h^{-1}}$ of water vapour (P. Spalart, private communication). If we consider the temperature contribution alone (the first term in equation (2.1)) we obtain $\Delta\varepsilon_r = -2.1 \times 10^{-4}$. This is roughly two orders of magnitude greater than

for the density variation in each vortex and for atmospheric density stratification and would lead to a 40 dB greater radar cross-section. However, Gilson (1992) reports that the wake RCS at 1 km behind the plane did not change when the engines were run at idle or full power. This is probably due to turbulent mixing of the exhaust with the ambient. Diversion of some engine exhaust into the laminarizing flow of the vortex cores may allow the exhaust to maintain its heat further downstream.

To estimate the contribution of water vapour in the exhaust, we use the upper value of 6000 lb h^{-1} per engine and assume an exhaust diameter of 2 m. This yields a partial pressure of vapour equal to 1.1 mb and a contribution of $\Delta\varepsilon_r$ of 3.7×10^{-6} which is much smaller than that due to temperature.

8. Summary and suggestions for future work

We will confine our closing remarks to three aspects: (1) the scattering analysis; (2) reflectivity of the density gradient in each vortex; (3) reflectivity of the wake in a stratified atmosphere.

(1) Whenever the index of refraction has a correlation length (in any cross-beam direction) that is comparable to or larger than the beamwidth (as is true for our two-dimensional models), it becomes necessary to *a priori* include the variation in beam amplitude. In addition, one has to use the far-field Green's function and retain sphericity of the incident wavefronts, the two being equally important (conditions under which these requirements may be disregarded are mentioned herein). In a real wake, the axial correlation length of the refractive index will be large initially, may decrease if turbulence develops (which is less likely within the vortex cores), and will ultimately tend towards the value for the ambient atmospheric turbulence as the wake dissipates. The more general analysis undertaken here may be called for during one or more of these stages. The character of the solutions of the more general analysis suggests that the Bragg condition from Tatarski's analysis remains a valid guiding principle; however, a methodical study of this should be made. We followed Tatarski in invoking the weak scattering approximation, but limit frequencies estimated for its validity were exceeded for many results we presented. Is strong scattering really important here?

(2) The point of this work was to answer the following question: are aircraft wakes sufficiently reflective to radar that they may be detected with reasonable powers at ranges appropriate to air traffic control and at frequencies not affected by precipitation? We observed that the density gradient in the vortex core scatters at 50 MHz, a frequency low enough that clutter due to precipitation is not an issue. Many radars used for atmospheric profiling are designed for this frequency so a test should be possible. The powers required for such radars to detect the vortex cores appear to be modest but some developments need to occur before they can provide a method for vortex detection in the context of air traffic control. These include beam scanning, reduction of minimum range, improvement of range resolution, and mitigation of the deleterious effects of core waviness on reflectivity.

(3) Transport of air within an oval in a non-adiabatic atmosphere provides a mechanism for scattering that dominates over vortex core reflectivity at frequencies somewhat higher than 50 MHz. We employed this mechanism to calculate radar cross-sections measured in an experiment and the results were of the right magnitude. However, the present two-dimensional model gave a sharp cut-off in reflectivity away from normal incidence, a feature not present in the experiments. Estimates indicated that in the experiment the oval boundary was very likely turbulent due to

both Kelvin–Helmholtz and centrifugal instabilities, and this may account for the difference. A computational study of this turbulence would be important not only from the standpoint of radar scattering but also to predict the rate of wake descent in a stratified atmosphere. Since stratification has seasonal, diurnal and geographic variations, its use as a basis for wake detection would have to be combined with atmospheric measurements and would be unusable in neutral conditions. Finally, the present work considered interaction of the wake with a calm atmosphere having only a mean refractive index gradient. Interaction of the wake with pre-existing turbulent fluctuations (Gilson, private communication) of refractive index could also be important under certain conditions.

We thank Drs W. Gilson and P. Ingwersen for providing us with raw data and other information on the experiment, Dr P. Spalart for suggesting that we account for density variation inside a vortex core and for supplying the information referred to in the text. Thanks are also due to Professor J. Jimenez for suggesting the inclusion of water vapour in the refractive index and to Dr M. Wang for help with integrals. Finally, the comments of two anonymous referees were useful.

Appendix A. The electric field in the incident beam: $\boldsymbol{E}_{\mathrm{i}}(x, y, z)$

The incident field is obtained using aperture antenna analysis (Silver 1949) where the far diffraction field is derived from the field on a surface (the 'aperture') near the antenna. We shall take the aperture to be circular.

For convenience we use a coordinate system (x, y, z) centred on the aperture. The plane of the aperture is x, y and z is normal to the aperture. These coordinates should not be confused with those in the rest of the paper where they refer to wake coordinates and where (x^*, y^*, z^*) refer to aperture coordinates.

A.1. *Conical beam*

The electric field created in the far zone by a plane aperture A on which the electric field is specified to be $\boldsymbol{E} = E_x^a(\boldsymbol{x}')\hat{\boldsymbol{x}}$ is (Silver 1949, p. 167, equation 124):

$$\boldsymbol{E}_{\mathrm{i}}(\boldsymbol{x}) = \frac{\mathrm{i}k}{4\pi r}\hat{\boldsymbol{x}}\mathrm{e}^{\mathrm{i}kr}(1+\cos\theta)\int_A E_x^a(\boldsymbol{x}')\mathrm{e}^{\mathrm{i}k\boldsymbol{x}'\cdot\boldsymbol{x}/|\boldsymbol{x}|}\,\mathrm{d}\boldsymbol{x}'. \tag{A 1}$$

Here (r, θ) are the spherical polar coordinates of $\boldsymbol{x}$, θ being the polar angle measured from the z-axis. Equation (A 1) is derived starting from vector Kirchhoff integrals and introducing several approximations valid in the limit of small wavelength compared to aperture diameter in which case the significant portion of the energy is confined to small θ. In addition, the phase of the field on the aperture has been assumed to be constant.

For an axially symmetric distribution of E_x^a on the aperture the integral in (A 1) becomes

$$I_A = 2\pi\int \varrho'\mathrm{d}\varrho' E_x^a(\varrho')J_0(k\varrho'\sin\theta), \tag{A 2}$$

where $\varrho' = \sqrt{x'^2 + y'^2}$. Two aperture illuminations are considered. For the case of uniform illumination:

$$E_x^a(\varrho) = \begin{cases} E_0, & \varrho \leqslant \varrho_a, \\ 0, & \text{otherwise}, \end{cases} \tag{A 3}$$

we obtain

$$I_A = 2\pi E_0 \varrho_a^2 \frac{J_1(k\varrho_a \sin\theta)}{k\varrho_a \sin\theta}. \tag{A 4}$$

For the case of Gaussian illumination of the aperture

$$E_x^a(\varrho) = E_0 \exp(-(\varrho/\sigma_\mathrm{a})^2), \tag{A 5}$$

we obtain

$$I_A = \pi {\sigma_\mathrm{a}}^2 E_0 \exp(-\tfrac{1}{4}k^2 {\sigma_\mathrm{a}}^2 \sin^2\theta), \tag{A 6}$$

thanks to Gradshteyn & Ryzhik (1980, p. 717, 6.63.4).

To calculate the radar cross-section according to (1.2) requires the maximum value at the target of the time-averaged power flux $\boldsymbol{S}_\mathrm{i} = \frac{1}{2}\mathrm{Re}\{\boldsymbol{E}_\mathrm{i} \times \boldsymbol{H}_\mathrm{i}^*\}$, where $\boldsymbol{H}_\mathrm{i}$ can be obtained from the Maxwell equation $\boldsymbol{H}_\mathrm{i} = 1/(\mathrm{i}\omega\mu_0)\nabla \times \boldsymbol{E}_\mathrm{i}$. If in evaluating $\nabla \times \boldsymbol{E}_\mathrm{i}$ from (A 1) we retain only the leading-order term ($O(1/r)$) and introduce $\mu_0 = 1/(c^2\varepsilon_0)$ we obtain

$$\boldsymbol{S}_\mathrm{i} = \tfrac{1}{2}c\varepsilon_0 (E_x^\mathrm{i})^2 \frac{z}{r}\hat{\boldsymbol{z}}, \tag{A 7}$$

where E_x^i denotes the x component of $\boldsymbol{E}_\mathrm{i}$. The radar cross-section is independent of the amplitude E_0 since both incident and scattered powers are proportional to E_0^2. For convenience, we chose

$$E_0 = \begin{cases} 2R_\mathrm{t}/(\mathrm{i}k\varrho_a^2) & \text{for uniform aperture illumination,} \\ 2R_\mathrm{t}/(\mathrm{i}k{\sigma_\mathrm{a}}^2) & \text{for Gaussian aperture illumination,} \end{cases} \tag{A 8}$$

in order to make equal to $\mathrm{e}^{\mathrm{i}kR_\mathrm{t}}$ the maximum value of E_x^i with respect to θ at fixed $r = R_\mathrm{t}$. The denominator in (1.2) is then

$$\text{maximum power density in incident beam at target} = \tfrac{1}{2}c\varepsilon_0. \tag{A 9}$$

In the calculations, instead of specifying the aperture radius as the input parameter, we specify the half-beamwidth θ_b and from it calculate the implied value of ϱ_a. For the Gaussian beam θ_b is defined to be where I_A drops to e^{-1} of its peak value and for the Bessel beam it is defined to be the location of the first zero thus giving

$$\varrho_a = \frac{3.83171}{k \sin\theta_\mathrm{b}}, \quad \sigma_\mathrm{a} = \frac{2}{k \sin\theta_\mathrm{b}}. \tag{A 10}$$

A.2. *Approximate cylindrical beam*

The cylindrical beam for the approximate scattering analysis in § 4 is obtained after introducing four approximations in (A 1) and (A 2): (*a*) replace $\cos\theta$ by 1 assuming small angular beamwidth; (*b*) replace r in the denominator by a constant range R_t; (*c*) replace $\sin\theta = u/r$ by u/R_t, where $u = \sqrt{x^2 + y^2}$ is the normal distance from the beam axis; (*d*) replace $\mathrm{e}^{\mathrm{i}kr}$ with $\mathrm{e}^{\mathrm{i}kz}$. Approximations (*b*) and (*c*) are valid when the relative change in beam width across the near and far ranges of the target is small. For approximation (*d*), however, a condition similar to the the far-field condition (1.6) must hold:

$$\epsilon_{(\mathrm{d})} = \frac{\pi L_\mathrm{s}^2}{\lambda R_\mathrm{t}} \ll 1. \tag{A 11}$$

Introducing these approximations into (A 1) gives

$$\boldsymbol{E}_\mathrm{i} = \frac{ik}{2\pi R_\mathrm{t}} \hat{\boldsymbol{x}} \mathrm{e}^{\mathrm{i}kz} I_A. \tag{A 12}$$

Substituting (A 4) and (A 6) for I_A into (A 12), using (A 10) and substituting values of E_0 from (A 8) we obtain

$$\boldsymbol{E} = \hat{\boldsymbol{x}} \mathrm{e}^{\mathrm{i}kz} \frac{2J_1(u/\sigma)}{u/\sigma}, \tag{A 13}$$

$$\sigma \equiv R_\mathrm{t} \sin\theta_\mathrm{b}/3.8371 \tag{A 14}$$

for the Bessel function beam and

$$\boldsymbol{E} = \hat{\boldsymbol{x}} \mathrm{e}^{\mathrm{i}kz} \exp(-u^2/\sigma^2), \tag{A 15}$$

$$\sigma \equiv R_\mathrm{t} \sin\theta_\mathrm{b} \tag{A 16}$$

for the Gaussian beam. For the incident power flux in the cylindrical beam we use the value (A 9) for the original conical beam.

Appendix B. Scattering of a pulse

Since the scattering problem is linear, treatment of a pulse is simply a matter of Fourier superposition of the results of the time-harmonic analysis.

We begin by reducing the original vector problem to a scalar problem. This will provide the set-up for using formulae already derived in Ishimaru (1978). For the time-harmonic analysis the incident electric field (A 1) has the form

$$\bar{\boldsymbol{E}}_\mathrm{i}(\boldsymbol{x}, t; \omega) = \hat{\boldsymbol{x}} \mathrm{Re}[F_\mathrm{i}(\boldsymbol{x}, \omega) \mathrm{e}^{-\mathrm{i}\omega t}]. \tag{B 1}$$

As in Appendix A we are using $\boldsymbol{x}$ to denote aperture coordinates. We assume the same spatial dependence for the magnetic field:

$$\bar{\boldsymbol{H}}_\mathrm{i}(\boldsymbol{x}, t; \omega) = c\varepsilon_0 \hat{\boldsymbol{y}} \mathrm{Re}[F_\mathrm{i}(\boldsymbol{x}, \omega) \mathrm{e}^{-\mathrm{i}\omega t}]. \tag{B 2}$$

According to Maxwell's equations $\bar{\boldsymbol{E}}$ is related to the curl of $\bar{\boldsymbol{H}}$ and therefore $\bar{\boldsymbol{E}}$ and $\bar{\boldsymbol{H}}$ should in general have different spatial dependence. However, to the extent that the wavelength is much smaller than the beamwidth, derivatives of $F_\mathrm{i}(\boldsymbol{x}, \omega)$ normal to the beam axis will be much smaller than derivatives along the beam and the forms (B 1) and (B 2) will nearly satisfy Maxwell's equations and be divergence free.

Henceforth we will write the incident field as a function of time only, taking it to be evaluated at the point $\boldsymbol{x} = (0, y_0, 0)$ where the beam centreline intersects the centreplane of the target. By a Fourier synthesis of (B 1) and (B 2) in time an arbitrary L_2 time dependence can be constructed:

$$\bar{\boldsymbol{E}}_\mathrm{i}(t) = \hat{\boldsymbol{x}} \mathrm{Re}[u_\mathrm{i}(t) \mathrm{e}^{-\mathrm{i}\omega_0 t}], \tag{B 3}$$

$$\bar{\boldsymbol{H}}_\mathrm{i}(t) = c\varepsilon_0 \hat{\boldsymbol{y}} \mathrm{Re}[u_\mathrm{i}(t) \mathrm{e}^{-\mathrm{i}\omega_0 t}], \tag{B 4}$$

where we have chosen to write the time dependence as the product of a carrier $\mathrm{e}^{-\mathrm{i}\omega_0 t}$ and a complex modulation $u_\mathrm{i}(t)$. The complex modulation is itself written as a product:

$$u_\mathrm{i}(t) = f(t) \mathrm{e}^{\mathrm{i}\phi(t)}, \tag{B 5}$$

where $f(t)$ and $\phi(t)$ are real and describe amplitude and phase modulation, respectively.

We now assume that for the time-harmonic analysis, the scattered field evaluated at the receiver is also of the form (B 1) and (B 2) with F_i replaced by F_s. This was verified to be true from the numerical results. Therefore by Fourier superposition

$$\bar{\boldsymbol{E}}_\mathrm{s}(t) = \hat{\boldsymbol{x}} \mathrm{Re}[u_\mathrm{s}(t) \mathrm{e}^{-\mathrm{i}\omega_0 t}], \tag{B 6}$$

$$\bar{\boldsymbol{H}}_\mathrm{s}(t) = c\varepsilon_0 \hat{\boldsymbol{y}} \mathrm{Re}[u_\mathrm{s}(t) \mathrm{e}^{-\mathrm{i}\omega_0 t}]. \tag{B 7}$$

The incident and scattered fields thus depend only on the scalar functions $u_i(t)$ and $u_s(t)$ and we are thus set-up to use Ishimaru's (1978, vol. 1, p. 94) discussion for scattering by a pulse. Using the fact that scattering is a linear and causal problem, Ishimaru derives the following 'input/output' relation for the complex modulation of the scattered pulse in terms of the modulation of the incident pulse:

$$u_s(t) = \int_{-\infty}^{\infty} U_i(\omega) H(\omega + \omega_0, t)\, e^{-i\omega t}\, d\omega, \tag{B 8}$$

where

$$U_i(\omega) = \frac{1}{2\pi} \int_{-\infty}^{\infty} u_i(t)\, e^{i\omega t}\, dt. \tag{B 9}$$

$H(\omega, t)$ has the interpretation that if $u_i(t) = 1$ (i.e. we have the time-harmonic case) then $u_s(t) = H(\omega_0, t)$. In the time-harmonic analysis we chose the incident field to have a normalization such that $u_i(t) = \exp(ikR_t)$. Hence $H(\omega_0, t)$ is simply the u_s we calculate in the time-harmonic analysis divided by $\exp(ikR_t)$. Since we have considered a steady target, thus losing the doppler effect, $H(\omega_0, t)$ does not depend on time.

It is instructive to obtain the form of the returned pulse implied by the approximate analysis. For backscattering at normal incidence and using the asymptotic form of the Bessel function for large ka, equations (4.25) and (4.33) give

$$\boldsymbol{E}_s(\boldsymbol{x}) = \hat{\boldsymbol{x}} \frac{\exp(ik(R_t + R_r))}{4R_r} (ka)^{1/2} \sigma \Delta \varepsilon_r^0 \cos(2ka - \tfrac{3}{4}\pi) \tag{B 10}$$

The bandwidth of the pulse is typically small compared to the centre frequency and so ka can be considered to be constant when outside the cosine. Hence, over the bandwidth of the pulse

$$H(\omega) = A \exp(ikR_r) \cos(2ka - \tfrac{3}{4}\pi), \quad k = \omega/c, \tag{B 11}$$

where

$$A = \frac{\Delta \varepsilon_r^0 \sigma (k_0 a)^{1/2}}{4R_r} \tag{B 12}$$

is a real constant independent of ω, and k_0 is the wavenumber corresponding to the centre frequency. Substituting the form (B 11) into the input/output relation (B 8) gives the complex modulation $u_s(t)$ of the returned pulse. When this is substituted into (B 6) one obtains

$$\begin{aligned} \bar{\boldsymbol{E}}_s(t) = \hat{\boldsymbol{x}} |A|/2 \{ & f(t'_-) \cos[\phi(t'_-) - \omega_0 t'_- + \phi_A - \tfrac{3}{4}\pi] \\ & + f(t'_+) \cos[\phi(t'_+) - \omega_0 t'_+ + \phi_A + \tfrac{3}{4}\pi] \}, \end{aligned} \tag{B 13}$$

where

$$t'_- = t - \frac{R_r}{c} - \frac{2a}{c}, \quad t'_+ = t - \frac{R_r}{c} + \frac{2a}{c}, \tag{B 14}$$

a is the radius of the oval, and ϕ_A is the phase angle of A. Equations (B 13) and (B 14) have the following interpretation. The returned pulse consists of the incident pulse reflected twice, each time with reflection coefficient $A/2$ and phase shifts $\phi_A = \pm 3\pi/4$. The two reflections occur at $z = \pm a$. The time shift $-R_r/c$ accounts for the travel time from the point $z = 0$ to the receiver while the additional time shifts $\pm 2a/c$ account for the round-trip time required to travel from $z = 0$ and the two points $z = \pm a$.

For the Born analysis the received pulse was obtained using the following procedure. First, $H(\omega)$ was obtained from the time-harmonic analysis for ω spanning an interval

($\Delta\omega$) consisting of few pulse bandwidths about the centre frequency. A convenient auxiliary quantity $T(\omega)$ was calculated such that

$$H(\omega, t) = \frac{T(\omega)\exp(\mathrm{i}kR_\mathrm{r})}{R_\mathrm{r}}. \tag{B 15}$$

Next $T(\omega)$ was multiplied by a Hanning window and Fourier analysed such that

$$T(\omega) = \sum_m \hat{T}_m \exp\left[\mathrm{i}\frac{2\pi}{\Delta\omega}m(\omega - \omega_0)\right]. \tag{B 16}$$

Knowing the coefficients $\hat{T}_m$ one can obtain the complex modulation of the received signal by substituting (B 16) and (B 15) into (B 8):

$$u_\mathrm{s}(t) = \frac{1}{R_\mathrm{r}}\sum_m \hat{T}_m u_\mathrm{i}\left(t - \frac{R_\mathrm{r}}{c} - \frac{2\pi m}{\Delta\omega}\right). \tag{B 17}$$

Rectangular and Gaussian forms of unit amplitude were implemented for the amplitude modulation:

$$f(t) = \begin{cases} 1, & |t| \leqslant \tau/2, \\ 0, & \text{elsewhere} \end{cases}, \qquad f(t) = \exp(-t^2/\tau^2), \tag{B 18}$$

where τ is the pulse duration. In this paper only the results for the Gaussian pulse are plotted since the rectangular pulse gave very close RCS results (within 0.25 dB for a few spot checks). For FM a linear frequency variation (chirp) was considered:

$$\phi(t) = \pi\alpha t^2. \tag{B 19}$$

Within the pulse width, the spread Δf_FM in the local frequency is

$$\Delta f_\mathrm{FM} = |\alpha|\tau. \tag{B 20}$$

The sign of α (up-chirp vs. down-chirp) was found to not matter. Table 2 gives τ and Δf_FM for the tests at Kwajalein.

The instantaneous power flux density vector associated with the incident pulse (B 3) and (B 4) is

$$\bar{\boldsymbol{S}}_\mathrm{i} = \bar{\boldsymbol{E}}_\mathrm{i} \times \bar{\boldsymbol{H}}_\mathrm{i} = \hat{\boldsymbol{z}}c\varepsilon_0 f^2(t)\cos^2(\phi(t) - \omega_0 t). \tag{B 21}$$

Finally, the instantaneous scattered power flux density vector associated with (B 6) and (B 7) is

$$\bar{\boldsymbol{S}}_\mathrm{s}(t) = \hat{\boldsymbol{z}}c\varepsilon_0|\boldsymbol{E}_\mathrm{s}(t)|^2. \tag{B 22}$$

From these we calculate an instantaneous RCS:

$$\mathrm{RCS}(t) = 4\pi R_\mathrm{r}^2 \frac{|\bar{\boldsymbol{S}}_\mathrm{s}(t)|}{|\bar{\boldsymbol{S}}_\mathrm{i}|_\mathrm{max}}. \tag{B 23}$$

REFERENCES

Bardina, J., Ferziger, J. H. & Rogallo, R. S. 1985 Effect of rotation on isotropic turbulence: computation and modeling. *J. Fluid Mech.* **154**, 321–336.

Batchelor, G. K. 1967 *An Introduction to Fluid Dynamics*. Cambridge University Press.

Betchov, R. & Szewczyk, A. 1963 Stability of a shear layer between parallel streams. *Phys. Fluids* **6**, 1391–1396.

Campbell, S. D., Dasey, T. J., Freehart, R. E. *et al.* 1997 Wake vortex field measurement program at Memphis, Tennessee, Data Guide. *NASA Contractor Rep.* 201690.

Carlon, H. R. 1970 Infrared emission by fine water aerosols and fogs. *Appl. Opt.* **9**, 2000–2006.

Chadwick, R. B., Jordan, J. & Detman, T. 1984 Radar cross section measurements of wingtip vortices. *Proc. ESA IGARSS 1984*, vol. 1, pp. 479–483. Also published as ESA SP-215.

Crow, S. C. 1970 Stability theory for a pair of trailing vortices. *AIAA J.* **8**, 2172–2179.

Crow, S. C. 1974 Motion of a vortex pair in a stably stratified fluid. *Poseidon Research Rep.* No. 1, Santa Monica, CA.

Drazin, P. G. & Reid, W. H. 1981 *Hydrodynamic Stability*. Cambridge University Press.

Gilson, W. H. 1992 Radar measurements of aircraft wakes. *Project Rep.* AAW-11, Lincoln Lab., MIT, Lexington, Mass.

Gilson, W. H. 1994 Aircraft wake RCS measurement. In *NASA Contractor Rep.* 10139, Part 2, pp. 603–623.

Gradshteyn, I. S. & Ryzhik, I. M. 1980 *Table of Integrals, Series and Products*. Academic.

Hannon, S. M. & Thomson, J. A. 1994 Aircraft wake vortex detection and measurement with pulsed solid-state coherent laser radar. *J. Mod. Opt.* **41**, 2175–2196.

Harmon, J. K., Slade, M. A., Vélez, R. A. *et al.* 1994 Radar mapping of Mercury's polar anomalies. *Nature* **369**, 213–215.

Iannuzzelli, R. J., Schemm, C. E., Marcotte, F. J. *et al.* 1998 Aircraft wake detection using bistatic radar: analysis of experimental results. *Johns Hopkins Appl. Phys. Lab. Tech. Digest* **19**, 299–314.

Ishimaru, A. 1978 *Wave Propagation and Scattering in Random Media*. Academic.

Jackson, J. D. 1962 *Classical Electrodynamics*. John Wiley & Sons.

Kingsley, S. & Quegan, S. 1992 *Understanding Radar Systems*. McGraw-Hill.

Köpp, F. 1994 Doppler lidar investigation of wake vortex transport between closely spaced parallel runways. *AIAA J.* **32**, 805–810.

Landman, M. J. & Saffman, P. G. 1987 The three-dimensional instability of strained vortices in a viscous fluid. *Phys. Fluids* **30**, 2339–2342.

Leblanc, S. & Cambon, C. 1997 On the three-dimensional instabilities of plane flows subjected to Coriolis force. *Phys. Fluids* **9**, 1307–1316.

Leonard, A., Rom-Kedar, V. & Wiggins, S. 1987 Fluid mixing and dynamical systems. *Nuclear Phys.* B *Proc. Suppl.* **2**, 179–190.

Leweke, T. & Williamson, C. H. K. 1998 Cooperative elliptic instability of a vortex pair. *J. Fluid Mech.* **360**, 85–119.

Marshall, R. E. & Myers, T. J. 1996 Wingtip generated wake vortices as radar targets. *IEEE AES Systems Magazine*, December 1996, pp. 27–30.

Milne-Thomson, L. M. 1968 *Theoretical Hydrodynamics*. Macmillan.

Nespor, J., Hudson, E., Stegall, R. & Freedman, J. 1994 Doppler radar detection of vortex hazard indicators. In *NASA Conf. Proc.* CP-10139, Part 2, pp. 651–688.

Noonkester, V. R. & Richter, J. H. 1980 FM-CW radar sensing of the lower atmosphere. *Radio Sci.* **15**, 337–353.

Ostro, S. J., Hudson, R. S., Nolan, M. C. *et al.* 2000 Radar observations of asteroid 216 Kleopatra. *Science* **288**, 836–839.

Ottersten, H. 1969 Atmospheric structure and radar backscattering in clear air. *Radio Sci.* **4**, 1179–1193.

Pedlosky, J. 1979 *Geophysical Fluid Dynamics*. Springer.

Perry, R. B., Hinton, D. A. & Stuever, R. A. 1997 NASA wake vortex research for aircraft spacing. *AIAA Paper* 97-0057.

Qin, J. H. 1998 Numerical simulations of a turbulent axial vortex. PhD thesis, School of Aeronautics and Astronautics, Purdue University.

Reid, R. C., Prausnitz, J. M. & Poling, B. E. 1987 *The Properties of Gases and Liquids*. McGraw-Hill.

Rennich, S. C. 1997 Accelerated destruction of aircraft wake vortices. PhD thesis, Dept. of Aero. & Astro., Stanford University. Also *Dept. of Aero. & Astro. Rep.* SUDAAR 705.

Risso, F., Corjon, A. & Stoessel, A. 1997 Direct numerical simulations of wake vortices in intense homogeneous turbulence, *AIAA J.* **35**, 1030–1040.

Rom-Kedar, V., Leonard, A. & Wiggins, S. 1990 An analytical study of transport, mixing and chaos in an unsteady flow. *J. Fluid Mech.* **214**, 347–394.

ROTH, K. R., AUSTIN, M. E., FREDIANI, D. J. *et al.* 1989 The Kiernan reentry measurements system on Kwajalein Atoll. *The Lincoln Lab. J.* **2**, 247–276.

RUBIN, W. L. 2000 Radar-acoustic detection of aircraft wake vortices. *J. Atmos. Ocean. Tech.* **17**, 1058–1065.

RUBIN, W. L., BURNHAM, D. C., SPITZER, E. A. & RUDIS, R. P. 2000 Robust low cost airport wake vortex sensor. *J. Aircraft* **37**, 377–382.

SILVER, S. 1949 *Microwave Antenna Theory and Design.* McGraw-Hill.

SKOLNIK, M. I. (Ed.) 1970 *Radar Handbook.* McGraw-Hill.

SPALART, P. R. 1996 On the motion of laminar wing wakes in a stratified fluid. *J. Fluid Mech.* **327**, 139–160.

SPALART, P. R. 1998 Airplane trailing vortices. *Annu. Rev. Fluid Mech.* **30**, 107–138.

SPALART, P. R. & WRAY, A. A. 1996 Initiation of the Crow instability by atmospheric turbulence. In *The Characterisation and Modification of Wakes from Lifting Vehicles in Fluids. Proc. Fluid Dynamics Panel Symp., Trondheim, Norway, May 1996.* AGARD CP-584, pp. 18-1–18-8.

TATARSKI, V. I. 1961 *Wave Propagation in a Turbulent Medium.* McGraw-Hill.

THAYER, G. D. 1974 An improved equation for the radio refractive index of air. *Radio Sci.* **9**, 803–807.

THOMAS, P. J. & AUERBACH, D. 1994 The observation of the simultaneous development of a long- and a short-wave instability mode on a vortex pair. *J. Fluid Mech.* **265**, 289–302.

VAN DYKE, M. 1982 *An Album of Fluid Motion.* Parabolic Press.

VINCENT, R. A. S., DULLAWAY, S., MACKINNON, A. *et al.* 1998 A VHF boundary layer radar: first results. *Radio Sci.* **33**, 845–860.

WIDNALL, S. E. 1975 The structure and dynamics of vortex filaments. *Annu. Rev. Fluid Mech.* **7**, 141–65.